

Chemical Signatures of AGB Mass Transfer in Gaia White Dwarf Companions

NATSUKO YAMAGUCHI ,¹ KAREEM EL-BADRY ,¹ HENRIQUE REGGIANI ,² RENÉ ANDRAE ,³ AND SAHAR SHAHAF ,³¹Department of Astronomy, California Institute of Technology, 1200 E. California Blvd, Pasadena, CA, 91125, USA²Gemini South, Gemini Observatory, NSF's NOIRLab, Casilla 603, La Serena, Chile³Max-Planck-Institut für Astronomie, Königstuhl 17, D-69117 Heidelberg, Germany

ABSTRACT

We present a homogeneous abundance analysis of 160 main-sequence stars in astrometric white-dwarf + main-sequence (WD+MS) binaries with orbits from Gaia DR3. These systems have AU-scale separations and are thought to have undergone mass transfer (MT) when the WD progenitor was an asymptotic giant branch (AGB) star. Using high-resolution spectroscopy, we measure chemical abundances of the MS stars, focusing on s-process elements. Since s-process nucleosynthesis occurs mainly in AGB stars, s-process enhancement in the MS star is a key signature of accretion from an AGB companion. We identify 40 barium dwarfs – 36 of them newly discovered – roughly doubling the known population in astrometric WD+MS binaries and extending it to lower metallicities than previously studied. The s-process abundances show large star-to-star variations that correlate with component masses and with metallicity but not with orbital separation. At the lowest metallicities, three barium dwarfs display strong CH and C₂ absorption bands, linking them to CEMP-s stars and implying that AGB mass transfer usually leads to strong carbon enhancement at low metallicity. By comparing the observed abundance patterns to AGB nucleosynthesis models, we show that the diversity of s-process enhancements can be explained by variations in donor mass, metallicity, and most importantly, the number of thermal pulses the AGB star experienced before the onset of MT. Variation in the depth of the accretors' convective envelopes, with which accreted material is diluted, strengthens correlations with MS star mass and metallicity. Our results establish Gaia WD+MS binaries as a powerful laboratory for constraining binary mass-transfer physics and the origins of chemically peculiar stars.

Keywords: Binary stars (154) — Chemical abundances (224) — White dwarf stars (1799) — Spectroscopy (1558) – Asymptotic giant branch stars (2100)

1. INTRODUCTION

Binaries hosting white dwarfs (WDs) and main sequence (MS) stars in close orbits (separations $a \lesssim 10$ AU) are end products of mass transfer (MT) processes that occurred when the WD progenitor was a giant. This makes WD+MS binaries observational probes of the physics of MT, which remains one of the most important unsolved problems in stellar physics and binary evolution.

The third data release (DR3) of the Gaia mission contained astrometric orbital solutions for over 160,000 binaries (Gaia Collaboration et al. 2023a,b). These solutions were obtained by fitting a Keplerian model to the wobble of unresolved binaries on the plane of the

sky due to orbital motion. Long-period orbits produce larger astrometric signals than short-period orbits, but orbits with periods significantly longer than the observational baseline (~ 1000 d in DR3) cannot be constrained astrometrically. As a result, DR3 astrometric orbits are sensitive to orbital periods (P_{orb}) ranging from roughly 100 to 1000 days. Using the DR3 astrometric orbit catalog, S. Shahaf et al. (2024) identified thousands of new WD+MS binary candidates. Most of them host $\sim 0.6 M_{\odot}$ WDs in AU-scale orbits, suggesting interaction with an asymptotic giant branch (AGB) donor (N. Hallakoun et al. 2024). While this is classically expected to lead to unstable mass transfer, their orbits are significantly wider than previously identified post-common envelope binaries (PCEBs) with $P_{\text{orb}} \lesssim 1$ d (e.g. M. Zorotovic et al. 2010, 2011; S. G. Parsons et al. 2015). Modeling of the selection function reveals that these AU-scale

systems are common but were disfavored by most discovery methods before Gaia (N. Yamaguchi et al. 2024b, 2025).

Several recent works have explored possible formation scenarios for AU-scale WD+MS binaries, finding that (1) MT from AGB donors may remain stable over a wider range of initial mass ratios than previously thought (based on “quasi-adiabatic” critical mass ratios derived by e.g. H. Ge et al. 2020; K. D. Temmink et al. 2023 in the general case of evolved donors), and (2) PCEBs may remain wide if MT begins during a thermal pulse of an AGB donor, when its envelope is very loosely bound (e.g. D. Belloni et al. 2024; N. Yamaguchi et al. 2024a,c, who studied the energy budget of the resulting common envelope in the context of the Gaia systems). Still, a formation model that can explain all of the distinctive traits of the Gaia post-MT systems (intermediate orbital separations, non-zero eccentricities, and a narrow WD mass distribution), as well as the sheer abundance of such systems, remains elusive.

One key observational signature of a previous MT phase is the presence of anomalous surface abundances. In particular, barium stars are stars with enhanced abundances of s-process elements, including but not limited to barium. Since the first studied barium stars were giants, the term “barium dwarfs” is commonly used for MS stars enhanced in s-process elements. As s-process nucleosynthesis is expected only to occur during the late stages of stellar evolution on the AGB, the abundances of these pre-AGB stars have been attributed to s-process enhanced material accreted from an AGB companion. Indeed, since their discovery, many barium stars have been confirmed to be in binary systems with WD companions (e.g. R. D. McClure et al. 1980; R. D. McClure 1983; A. Jorissen & M. Mayor 1988).

Another closely related population is the carbon enhanced metal-poor (CEMP) stars found in the Galactic halo, with typical abundances of $[\text{Fe}/\text{H}] \lesssim -2.0$ and $[\text{C}/\text{Fe}] \gtrsim 0.7$ (e.g. S. Rossi et al. 1999; T. C. Beers & N. Christlieb 2005; W. Aoki et al. 2007a). A large fraction of CEMP stars are also s-process enhanced, with $[\text{Ba}/\text{Fe}] \gtrsim 0.5$ (the so-called ‘CEMP-s’ stars; e.g. J. E. Norris et al. 1997; W. Aoki et al. 2007b; K. Jonsell et al. 2006; T. Masseron et al. 2010). Similar to most barium stars, the majority of CEMP-s stars reside in binaries (S. Lucatello et al. 2005) and thus, their s-process enhancement has also been attributed to mass transfer from AGB donors (C. Abate et al. 2015, 2018). However, compared to barium stars, CEMP-s stars are more pristine, meaning it is easier to disentangle signatures of metals originally present in their atmosphere and those of accreted material. They are also older, making them

unique probes of binary interactions in the early Universe (e.g. A. Arentsen et al. 2022).

Recently, P. Rekhi et al. (2024, 2025) compiled a sample of 38 systems with s-process enrichment in the Gaia sample of WD+MS binaries using a combination of GALAH archival spectra and their own follow-up spectra. They found that about 30% of WD+MS binaries in the Gaia sample are enhanced in s-process elements, but the s-process abundances are not strongly correlated with the binaries’ orbital parameters. They also identified an anti-correlation between s-process abundances and bulk metallicity in the sample.

In this paper, we expand on these works by targeting a larger sample of WD+MS binaries from the Gaia sample with high-resolution spectroscopy. We target sources with a broad range of metallicities, including several below $[\text{Fe}/\text{H}] = -2$, and also include several candidate MS + neutron star (NS) binaries. We identify 36 new barium dwarfs, and confirm 4 existing ones in the literature. We find evidence of significant carbon enhancement in three of the most metal-poor barium dwarfs, creating a link to CEMP-s stars. We also present a population model to explain the diversity of s-process abundances found in the Gaia WD+MS binary sample.

The remainder of this paper is organized as follows. In Section 2, we describe target selection for follow-up optical spectroscopy. In Section 3, we describe observations of these targets and the data reduction process. Section 4 details the analysis to constrain atmospheric parameters and measure chemical abundances. In Section 5, we discuss the relationships between the measured abundances and how they vary with the various properties of the systems. We also describe two barium dwarfs orbiting candidate NSs and three with evidence of strong carbon enhancement. In Section 6, we compare our barium dwarfs to several related populations of chemically peculiar stars in the literature. In Section 7, we use theoretical models of s-process yields in the AGB donors and consider the effect of convective mixing in the envelopes of the MS accretors to predict and explain the observed trends and scatter in the barium abundances with the stellar and orbital parameters. Finally, we conclude with a summary of our key findings in Section 8.

2. TARGET SELECTION

We selected targets from the sample of sources identified by S. Shahaf et al. (2024) as unlikely to be MS+MS binaries. Their selection relies on a quantity called the astrometric mass ratio function (AMRF), which can be

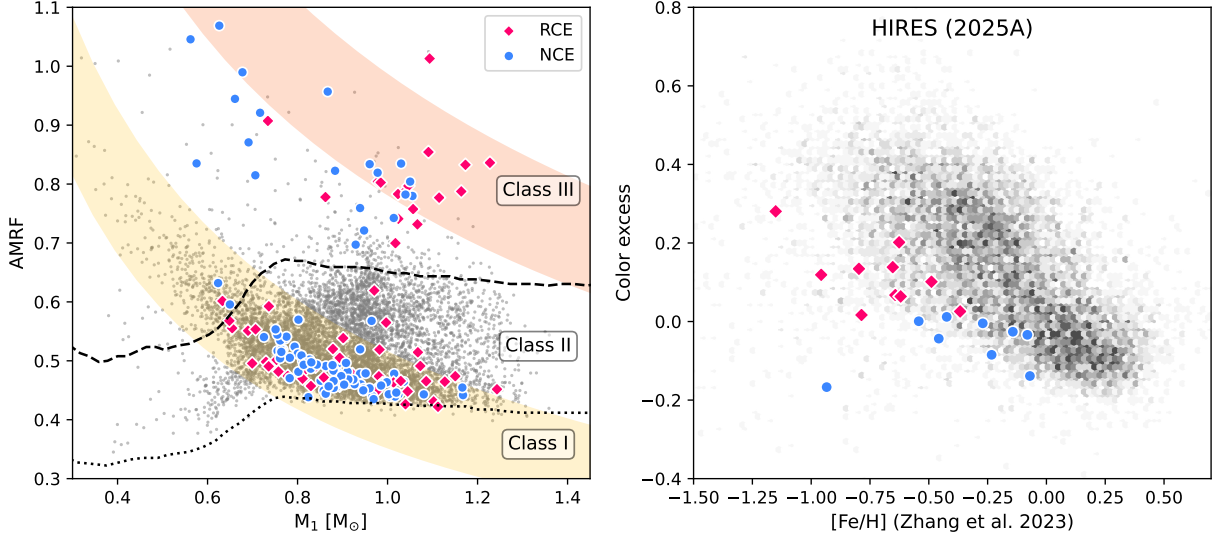


Figure 1. *Left:* AMRF versus luminous star mass, M_1 , for the full non-class I sample from S. Shahaf et al. (2024) (grey points). Our targets selected for follow-up are shown with colored points, separated by whether they were classified as NCE (pink diamonds) or RCE (blue circles) by S. Shahaf et al. (2024). The dotted and dashed lines are boundaries separating systems in the three classes (Section 2). The shaded regions corresponds to the expected locations of systems hosting dark compact object secondaries with masses between $0.45 - 0.75 M_\odot$ (yellow, lower) and $1.4 - 2.1 M_\odot$ (orange, upper), corresponding to typical WD and NS masses. While sources classified as NCE are less likely to be triples, we believe that both the NCE and RCE sources in our follow-up sample are dominated by compact object companions (see text). *Right:* Color excess against $[\text{Fe}/\text{H}]$ (Zhang et al. 2023) for non-class I systems. The two quantities are anti-correlated, meaning that the NCE sample is biased against metal-poor primaries. We selected several RCE systems lying below the densely populated strip in this space, which are likely to host WDs.

defined purely in terms of observables:

$$\text{AMRF} = \frac{\alpha}{\varpi} \left(\frac{M_1}{M_\odot} \right)^{-1/3} \left(\frac{P_{\text{orb}}}{\text{yr}} \right)^{-2/3} \quad (1)$$

where α is the angular photocentric semi-major axis, ϖ is the parallax, M_1 is the mass of the luminous star, and P_{orb} is the orbital period. As described by S. Shahaf et al. (2019), observed binaries can be grouped into three classes based on their location in the AMRF vs M_1 plane.

- Class-I: Orbit consistent with hosting a single MS secondary.
- Class-II: Orbit inconsistent with hosting a single MS secondary. May host an inner binary of two low-mass MS stars (forming a triple system), or a compact object contributing little to no light (most likely a cool WD, but also possibly a NS or black hole).
- Class-III: Orbit inconsistent with hosting a single MS companion or an inner binary containing two MS stars. Likely to host a compact object.

In our spectroscopic follow-up, we considered both class-II and III (i.e. “non-class-I”) systems. In the left

panel of Figure 1, we show our targets in the $\text{AMRF} - M_1$ plane. While restricting to only class-III systems would provide a purer sample of compact objects with less potential contamination from triples, this would also exclude the vast majority of systems hosting WDs, which have mass ratios too low to be class-III. Instead, in constructing their WD + MS binary catalog, S. Shahaf et al. (2024) removed potential triples in the class-II systems by implementing a color cut which excludes systems that appear redder than expected for a single MS star. They call the resulting sample the “No Color Excess (NCE)” sample. The remaining non-class I systems that do not pass this cut – meaning they are redder than predicted by a 2 Gyr-old isochrone at the same metallicity – are referred to as the “Red Color Excess (RCE)” sample.

We prioritized NCE candidates in our follow-up. However, many of our targets were selected from a preliminary, unpublished version of the S. Shahaf et al. (2024) sample, and were classified as NCE there but as RCE in the final sample. The preliminary and final samples differed in the adopted metallicities and color excess thresholds. We found that the final NCE selection of S. Shahaf et al. (2024) was conservative: most of the systems classified as RCE class-II in our sample are still likely to host WDs, as evidenced by their mass and eccentricity distributions. Moreover, the fact that many

of our class-III targets – which have AMRF values too large to be explained by triples – are nevertheless classified as RCE provides further evidence that many of the objects labeled as RCE are not actually triples.

Simulations from [N. Yamaguchi et al. \(2025\)](#) showed that while the cut on color excess effectively eliminates triples, it also removes about half of all systems hosting WDs in the non-class I sample (see their Figure 5). In particular, they found that the cut is biased against metal-poor systems, likely because the adopted 2 Gyr-old isochrones predict a relation between color and metallicity that is steeper than observed. This means that very few systems with $[\text{Fe}/\text{H}] < -0.5$ dex enter the NCE sample, suggesting that a metallicity-dependent cut on the color excess may be more appropriate than the flat cut adopted by [S. Shahaf et al. \(2024\)](#).

With this in mind, we selected several metal-poor systems to be observed with HIRES (Section 3) that are in the non-class I sample, but not in the NCE sample of [S. Shahaf et al. \(2024\)](#). As shown in the right panel of Figure 1, we selected metal-poor stars that lie below the average color excess at their metallicities.

In total, we observed 178 sources.

3. OBSERVATIONS

We obtained high-resolution spectra of targets through several different programs using three instruments over the course of two years, as described below.

3.1. FEROS

We obtained a total of 219 spectra of 92 targets using the Fiber-fed Extended Range Optical Spectrograph (FEROS; [A. Kaufer et al. 1999](#)) instrument installed on the MPG/ESO 2.2 m telescope at the La Silla Observatory (Programs 113.26XB, 114.27SS, and 115.28KE). Exposure times ranged from 600 to 2400 s, depending on the brightness of the target. We used 1×1 binning. This allowed us to achieve a spectral resolution $R \sim 50,000$ over 3860 to 6770 Å. For a single observation, the typical signal-to-noise ratio (SNR) achieved was ~ 25 and 15 above and below 5000 Å, respectively. We reduced the raw data using the CERES pipeline ([R. Brahm et al. 2017](#)).

3.2. MIKE

We obtained 54 spectra of 24 targets with the Magellan Inamori Kyocera Echelle (MIKE) spectrograph mounted on the Magellan Clay telescope at Las Campanas Observatory ([R. Bernstein et al. 2003](#)). We used the $0.7''$ slit with 2×2 binning, which resulted in a typical $R \sim 34,000$ and wavelength coverage of 3325–9680 Å. Exposure times ranged from 600 to 2400 s,

which yielded typical SNR for a single observation of ~ 50 and 40 above and below 5000 Å. We reduced the spectra with the MIKE Pipeline using CarPy ([D. D. Kelson et al. 2000; D. D. Kelson 2003](#)).

3.3. HIRES

We obtained 66 spectra of 61 targets with the High Resolution Echelle Spectrometer (HIRES) on the Keck I telescope. 34 of these targets were observed through the California Planet Search (CPS; [A. W. Howard et al. 2010](#)) queue, which allowed for more flexible scheduling. For all observations, we used the C2 decker ($0.86'' \times 14''$ slit) with 3×1 binning, yielding spectra with $R \sim 50,000$. For targets observed through CPS, our exposure times ranged from 120 to 1200 s and we used the HIRESr cross-disperser. This resulted in $\text{SNR} \sim 55$ and 35 above and below 5000 Å and wavelength coverage of 3640 – 6420 Å. For the other targets, we used a fixed exposure time of 1200 s and the HIRESb cross-disperser. This led to $\text{SNR} \sim 40$ and 35 above and below 5000 Å, and wavelength coverage 3840 – 6640 Å.

We reduced the raw data using the MAuna Kea Echelle Extraction (MAKEE) package, which extracts spectra from each echelle order, then carries out bias correction, background subtraction, and wavelength calibration.

We note that a subset of the MIKE and HIRES observations were originally made as part of a follow-up program of NS + MS binary candidates ([K. El-Badry et al. 2024b,c](#)), but were primarily used to measure radial velocities (RVs) rather than abundances.

3.4. Continuum normalization and RV correction

We processed all reduced spectra using the `iSpec` package ([S. Blanco-Cuaresma et al. 2014; S. Blanco-Cuaresma 2019](#)). To estimate the continuum for each echelle order, `iSpec` first applies a median and maximum filter to the data to mitigate noise effects and avoid strong absorption features, and then fits multiple splines of a specified degree to the data in each order to be used for the normalization. We chose typical window sizes of 0.05 nm and 1.0 nm for the median and maximum filters, respectively, and splines of degrees 4 and 5, but varied the exact choices for each order and instrument in order to optimize the continuum normalization and avoid overfitting ⁴. We then merged all orders of the normalized spectra, taking an inverse-variance weighted average of the flux in overlap regions. The RV of each spectrum was calculated with `iSpec`'s cross-correlation

⁴ For more details of this process, consult the `iSpec` manual: www.blancocuaresma.com/s/iSpec/manual/introduction

algorithm using a template solar spectrum. After shifting the spectra to rest frame, if repeated observations were taken for one target with the same instrument, we co-added them into one spectrum to increase SNR.

4. ANALYSIS

4.1. Atmospheric parameters with excitation/ionization balance

To measure equivalent widths (EWs) of absorption lines, we used `REvIEW`⁵ (M. McKenzie et al. 2022). Provided a spectrum and linelist, `REvIEW` fits a region $\pm 0.6 \text{ \AA}$ around the central wavelength of each line with up to three Gaussians to separate out contributions from closely spaced lines that may be partly blended.

We then use `q2`⁶ (I. Ramírez et al. 2014) to determine stellar parameters. This code is a python interface for `MOOG` (2019 release; C. A. Sneden 1973; C. Sneden et al. 2012) and calls the `abfind` function, which uses the excitation/ionization equilibrium method with the measured EWs of iron lines. This method determines the optimal set of effective temperature (T_{eff}), surface gravity ($\log(g)$), metallicity ([Fe/H]), and microturbulence (ξ) for which the inferred absolute iron abundance ($A(\text{Fe})$) from individual lines is independent of the lines' ionization states, excitation potentials (EP), and relative line strengths (i.e. reduced equivalent width, REW) (e.g. D. F. Gray 2008).

We remove lines with EW above 120 m\AA to avoid saturated lines, as well as those with EW below 10 m\AA , which we found to be dominated by noise. In cases with low SNR, we increased this lower bound to 20 m\AA . We use the MARCS atmosphere grid (B. Gustafsson et al. 2008) and by default, we fit all four stellar parameters. For the initial guess of T_{eff} , $\log(g)$, and [Fe/H], we used best-fit values obtained using the *Gaia* XP very low-resolution spectra, as described in R. Andrae et al. (2023). However, we do not use published results from R. Andrae et al. (2023) as they make use of parallaxes from the `gaia_source` catalog, which are derived from a single-star astrometric solution. Instead, we use re-calculated values using parallaxes from the `nss_two_body_orbit` table. For ξ , we use the empirical relation from I. Ramírez et al. (2013) (their Equation 5), derived for FGK MS stars.

For the majority of spectra (131 out of 178), the method described above leads to successful convergence of stellar parameters. In Appendix A.1, we show the excitation/ionization balance achieved for several objects

with both successful and problematic results. For successful cases, the inferred abundances depend minimally on line-specific properties.

The remaining spectra experience one or more of the following issues:

- i. Best-fit ξ goes to 0.
- ii. Best-fit $\log(g)$ goes to 5.0.
- iii. Convergence of stellar parameters is not achieved.

The first two issues are problematic as solvers are reaching the edge of the stellar atmosphere grid, making the results potentially unreliable. In addition, based on the position of our objects on the color-magnitude diagram (CMD), all primaries are expected to be MS stars with $\log(g) = 4 - 5$. These issues may be traced back to inaccurate EW measurements due to low-SNR spectra, spectra broadened by stellar rotation, and/or poor choice of parameter initialization. Moreover, some stars have few strong Fe II lines with reliable EWs, which can prevent a robust constraint on $\log(g)$. Additionally, ξ is known to be sensitive to various systematics – such as the SNR of the spectra, continuum placement, and line blending (e.g. A. Mucciarelli 2011; P. Jofré et al. 2014; S. Blanco-Cuaresma 2019).

In these cases, we fix ξ and/or $\log(g)$ to their initial values and rerun the fit, leaving the remaining parameters free. The majority of objects for which fixing $\log(g)$ was required were observed by FEROS, suggesting that the issue stems from their lower SNR compared to observations made with other instruments (Section 3).

In total, we obtain reliable stellar parameters for 160 targets. The remaining 18 targets have spectra that did not achieve convergence or resulted in qualitatively poor excitation/ionization balance. Some of these were obtained in poor conditions, resulting in abnormally low SNR, prohibiting accurate EW measurements. This is particularly problematic for metal-poor stars with few strong iron lines. A few stars also have broad lines indicative of rapid rotation, which can cause blending and erroneous EWs. The rest of our analysis is focused on the 160 sources with converged and reliable parameters.

4.2. Spectral fitting results

In the upper panels of Figure 2, we compare stellar parameters from our analysis to those calculated with the *Gaia* XP spectra using the method from R. Andrae et al. (2023). We find general agreement between the two works. However, there are two notable discrepancies. Below $\sim 5500 \text{ K}$, we find a roughly linearly increasing discrepancy in T_{eff} , where our estimates are

⁵ <https://github.com/madeleine-mckenzie/REvIEW>

⁶ <https://github.com/astroChasqui/q2>

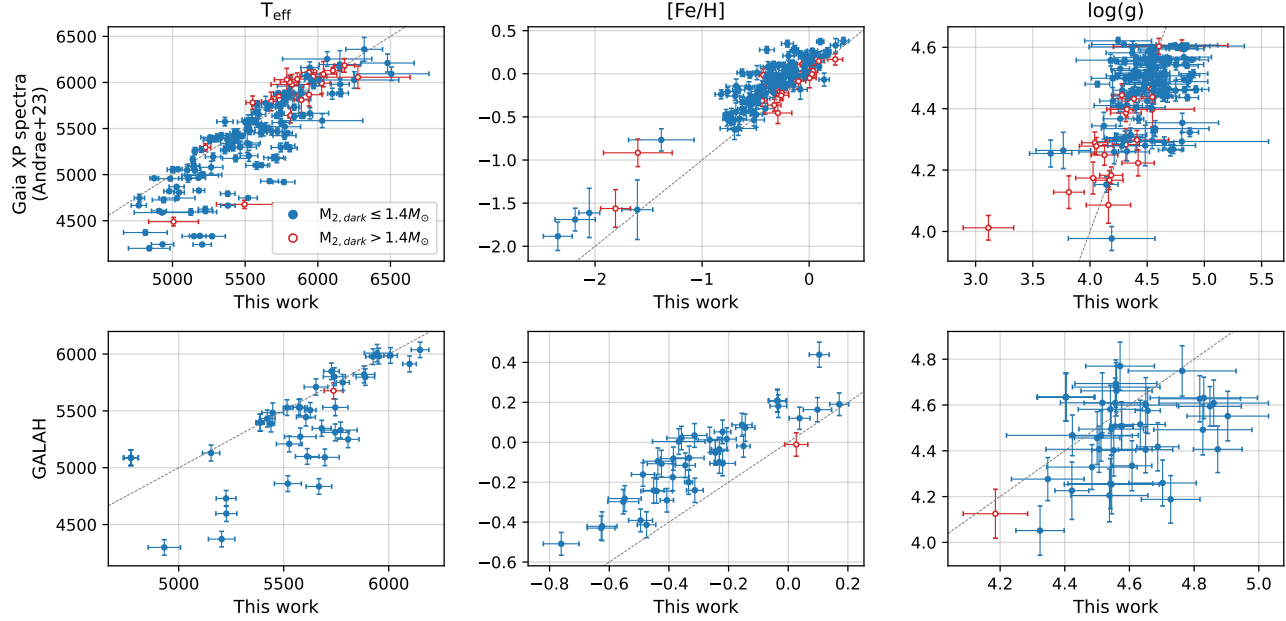


Figure 2. Comparison of best-fit stellar parameters obtained in this work (Section 4.1) with those calculated using Gaia low-resolution spectra (R. Andrae et al. 2023; top row), as well as those from GALAH DR4 (S. Buder et al. 2025; bottom row). Systems with secondary masses above and below the Chandrasekhar mass of $1.4 M_{\odot}$ are plotted with red unfilled and blue filled markers respectively.

consistently hotter. This is not unexpected given previous work which has also found that stellar parameters determined using different methods and codes tend to become more discrepant with each other at low temperatures (e.g. V. Hegedűs et al. 2023). We use the spectroscopic T_{eff} measurements throughout for consistency. In Appendix A.2 (Figure 16), we show that our conclusions about which sources have s-process enhancement are not sensitive to this choice.

In addition, our metallicities are systematically lower by 0.2 dex on average than those estimated by R. Andrae et al. (2023). One factor that may contribute to this is that R. Andrae et al. (2023) provides the mean metallicity, $[M/H]$, not $[\text{Fe}/\text{H}]$, meaning that it is not a one-to-one comparison. In particular, old stars deficient in iron ($[\text{Fe}/\text{H}] < -1.0$) are usually more enriched in other metals, such as α -elements (e.g. R. Cayrel et al. 2004; V. Z. Adibekyan et al. 2012) and carbon (e.g. H. Li et al. 2022), which would increase the average metal content.

For objects found in the fourth data release of the Galactic Archaeology with HERMES (GALAH) Survey (S. Buder et al. 2025), we also compare the quoted stellar parameters from this catalog (with quality flags `flag_sp = 0` and `flag_fe_h = 0`) to our results in the lower panels. We once again note an offset in $[\text{Fe}/\text{H}]$.

While these comparisons are helpful for validation, we emphasize that R. Andrae et al. (2023), GALAH, and our work all use distinct methods to estimate stellar pa-

rameters and metallicities (data-driven machine learning, synthetic spectral fitting with neural networks, and excitation/ionization balance, respectively) and different underlying radiative transfer codes, meaning systematic offsets are not unexpected (e.g. S. Blanco-Cuaresma 2019).

In Figure 3, we compare regions of the observed spectra for three objects to synthetic spectra generated using our best-fit T_{eff} , $\log(g)$, and $[\text{Fe}/\text{H}]$. We generated the synthetic spectra using the `iSpec` (S. Blanco-Cuaresma et al. 2014; S. Blanco-Cuaresma 2019), which provides a python interface through which we employed the SPECTRUM radiative transfer code⁷ (R. O. Gray & C. J. Corbally 1994). The projected rotational velocity was fixed to the solar value ($v \sin(i) = 1.6 \text{ km/s}$; e.g. Y. V. Pavlenko et al. 2012) and the resolution was set to 50,000. We did not vary individual elemental abundances when generating these models. We include these plots for objects observed with different instruments and at a range of metallicities to provide visual confirmation that the best-fit parameters obtained through our method described above are reasonable.

4.3. Deriving abundances

To measure elemental abundances, we once again use REview to measure EWs of lines for elements other than

⁷ <https://www.appstate.edu/grayro/spectrum/spectrum.html>

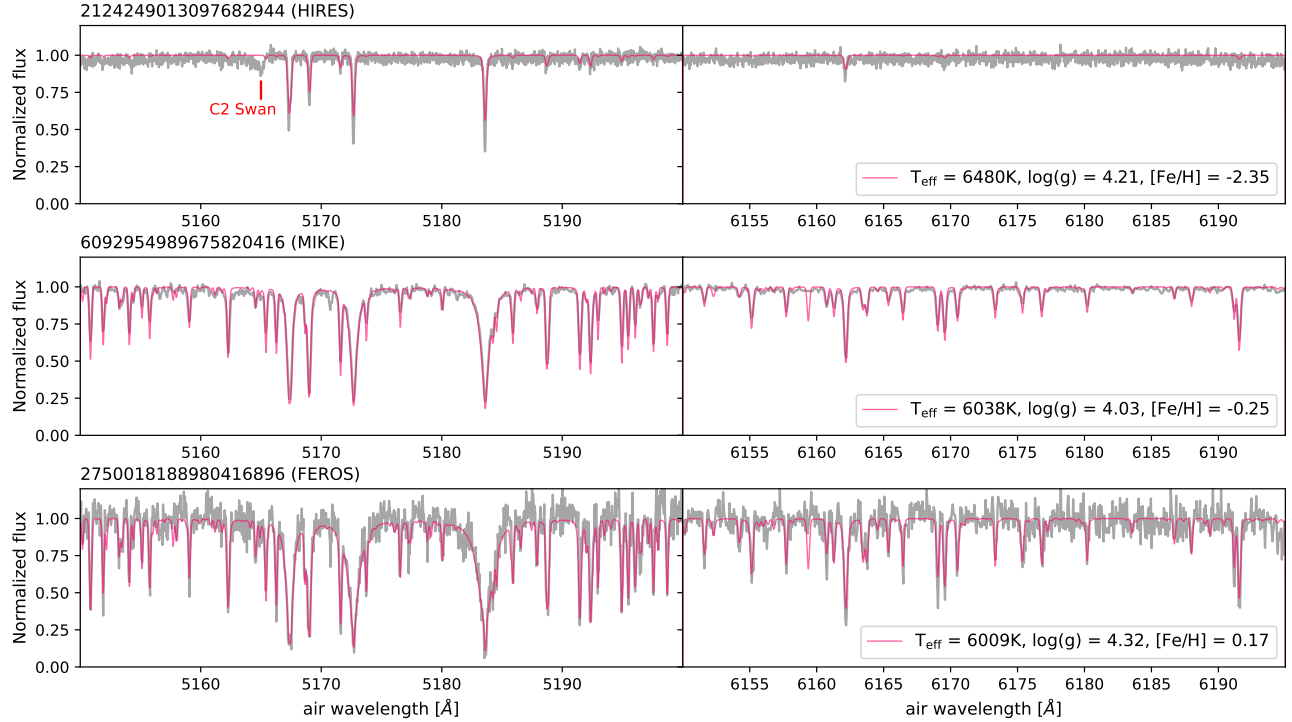


Figure 3. Observed spectra of three targets (gray) compared with synthetic spectra generated using their best-fit stellar parameters (pink; Section 4.1). We select targets covering a wide range of $[Fe/H]$ with similar T_{eff} and $\log(g)$, observed with different instruments. On the left, we plot the region around the magnesium triplet, and on the right, we move to redder wavelengths populated with iron lines. Visually, we see good agreement between the observations and the corresponding models, suggesting that our stellar parameters are reasonable. For the most metal-poor star (top row), the C₂ Swan band at 5165 Å is visible, which suggests carbon enhancement (Section 5.4).

iron. In Figure 4, we show Gaussian fits to strong barium and yttrium lines in a few example barium dwarfs.

Together with the best-fit stellar parameters determined above, the EWs are inputted into `q2`, which returns absolute abundances of specified elements inferred by each line. We consider lines with EWs between 20 and 180 mÅ. Compared to iron, we set a stricter lower bound to avoid the weakest lines where noise is being fit; while we set a less restrictive upper bound as there are fewer strong lines. Most elements of interest have at least one line with EW below this looser upper limit, and we have confirmed that the inferred abundances from individual lines with EWs above and below 120 mÅ are consistent, suggesting that saturation is not a major issue. In Table 1, we list key lines of elements used to determine their abundances which are discussed in Section 5. Note that we completely exclude several strong lines (e.g. Ba II $\lambda 4554\text{\AA}$) as these are often saturated, making their EWs uninformative.

For each element, we discard lines which have residuals of more than 0.3 dex from the median. Unless otherwise stated, we use solar abundances from M. Asplund et al. (2021) to calculate the differential abundances. Where there are multiple lines, the best-fit value is taken to be

the median of the abundances inferred from each line and the error is taken to be their standard deviation divided by the square root of the total number of lines. If only one line is measured, we set a fixed error of 0.2 dex. This is a conservative choice, being roughly the 90th percentile of the standard deviations of abundances with multiple lines.

We note that as expected, there is close agreement between $[FeI/H]$ and $[FeII/H]$ for most of our systems. However, approximately 17% of them have discrepancies between greater than 0.2 dex. Almost all of these are cases where $\log(g)$ was fixed to achieve convergence of stellar parameters (Section 4.1). Since $\log(g)$ is determined via ionization balance, this is unsurprising.

5. RESULTS

The resulting best-fit stellar parameters and abundances for all 160 objects are summarized in Tables 2 and 3 in Appendix A.3.

5.1. Abundance patterns

In Figure 5, we plot $\log(g)$ vs. T_{eff} as well as abundances of several α and s-process elements as a function of $[FeI/H]$. For reference, in the background, we

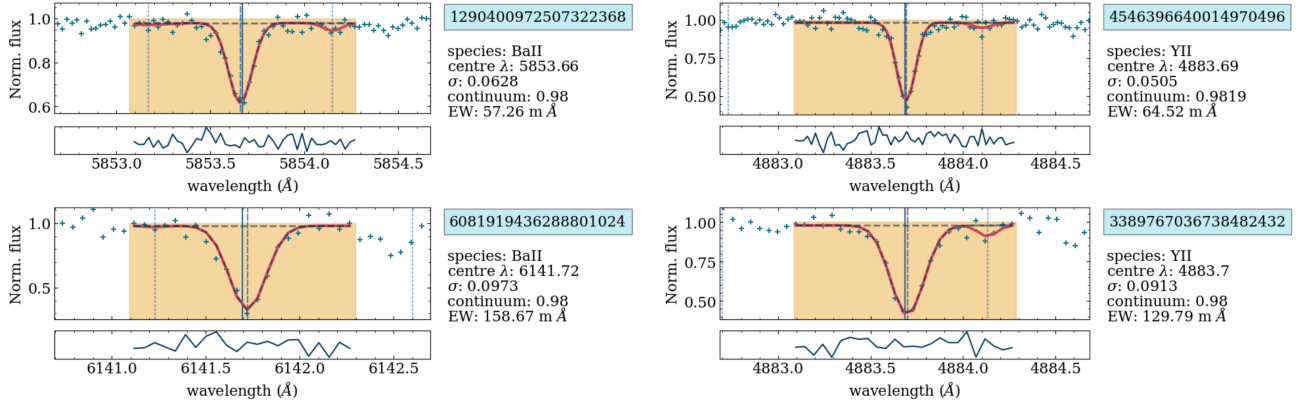


Figure 4. Examples of strong lines of singly ionized barium and yttrium. The fitting region is shaded in yellow, and the best-fit model is plotted in red. The solid vertical line indicates the position of the line center provided in the linelist, while the dashed and dotted lines indicate the minima of the fitted Gaussians. The upper two panels are fits to HIRES spectra, while the lower left and right are fits to FEROS and MIKE spectra.

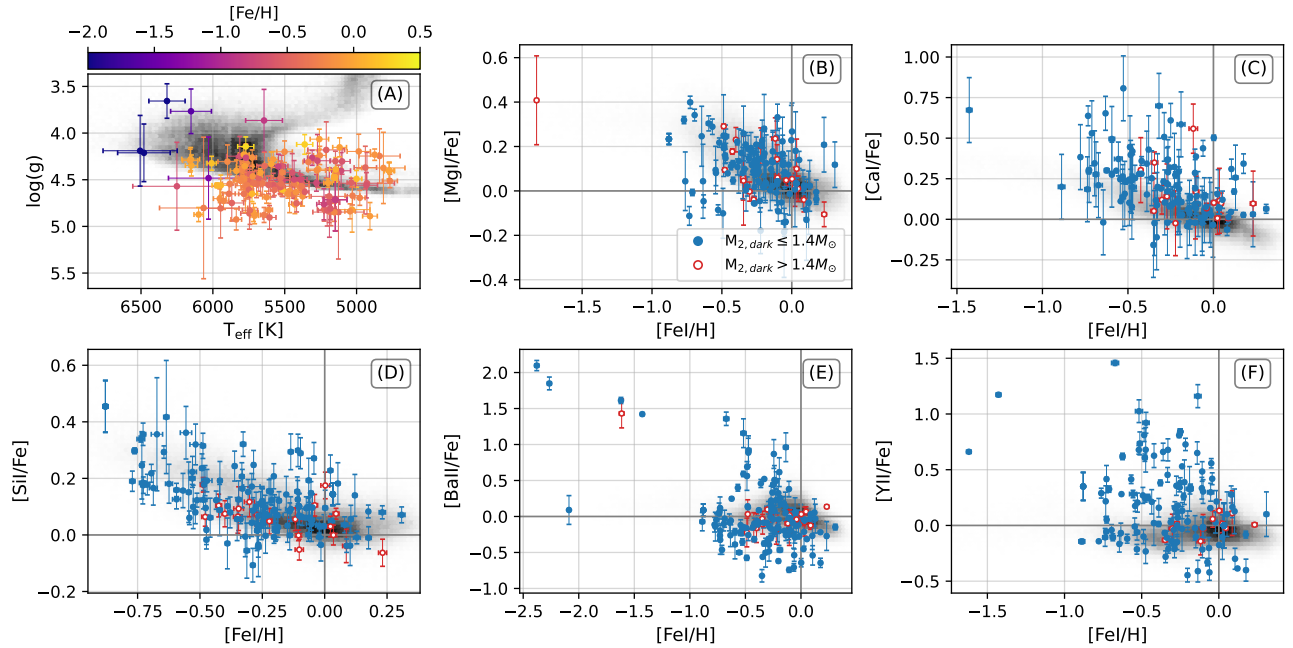


Figure 5. Atmospheric parameters (A) and derived abundances of various elements (B-F). In the background of each panel, we plot the distribution of the corresponding parameters for sources in the GALAH DR4 catalog. Panel (A) shows that as expected, all targets are consistent with being on the MS, with more metal-poor stars being hotter. Panels (B) - (D) show that the expected trends in the α -elements are seen in both GALAH and our sample. We target stars that likely accreted material from an AGB donor, explaining the greater fraction of stars that are rich in s-process elements, seen in panels (E) and (F).

plot distributions of the corresponding parameters for all sources in the GALAH DR4 catalog that satisfy the relevant quality cuts (`flag_X_fe = 0`, where X is the element of interest, as well as `flag_sp = 0` and `flag_fe_h = 0`). Systems with best-fit dark secondary masses below and above $1.4 M_{\odot}$ are plotted in blue and red, respectively.

Our sample lies on the expected region for MS stars in panel (A), with more metal-poor stars being hotter on average.

Panels (B) to (D) show α element abundances relative to iron, $[\alpha/\text{Fe}]$, against $[\text{FeI}/\text{H}]$. Our measured abundances follow the typical anti-correlation between $[\alpha/\text{Fe}]$ and $[\text{Fe}/\text{H}]$ observed in the Galactic disk (e.g. M. R. Hayden et al. 2015), with a high- α plateau at low $[\text{Fe}/\text{H}]$ due to rapid enrichment of stars formed at early

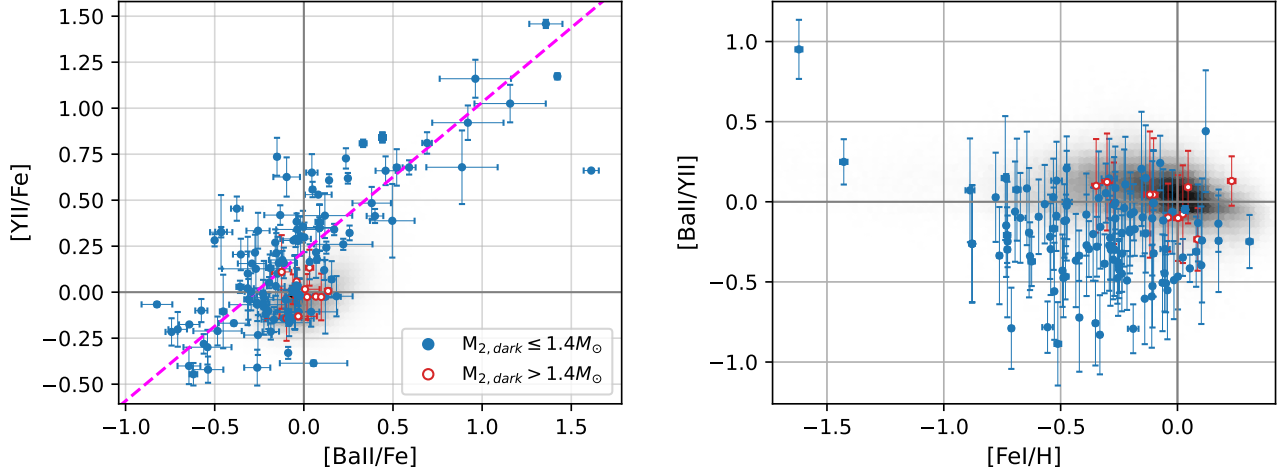


Figure 6. *Left:* Abundance of yttrium plotted against barium. Both elements are primarily produced by the s-process in AGB stars. Their abundances are strongly correlated. Only sources with $M_{2,\text{dark}} < 1.4 M_{\odot}$ are enhanced in both elements. The magenta line is a linear fit to the data. *Right:* Relative abundance of barium (a heavy s-process element) to yttrium (a light s-process element) as a function of metallicity. We find that all stars with $[\text{Fe}/\text{H}] > -1.0$ have $[\text{Ba}/\text{Y}] < 0$ to within 1 σ .

Element	Central wavelengths [Å]
Mg I	4730.04, 5711.09
Ca I	5867.56, 6499.65
Si I	5645.61, 5665.55, 5684.48, 5690.42, 5701.1, 5793.07, 6721.85
Ba II	5853.67, 6496.9
Y II	4854.87, 4883.69, 4900.11

Table 1. Lines of several elements of interest used to calculate abundances. All wavelengths are in air and rounded to two decimal places.

times by core collapse supernovae (e.g. E. Delgado Mena et al. 2017; S. Buder et al. 2021). This is one indication that our measured abundances are reasonable.

Lastly, in panels (E) and (F), we show abundances of singly ionized barium and yttrium. We see more complex structures in these panels that diverge from the trends seen for typical stars in GALAH DR4. In general, our sample has a larger fraction of stars that are enriched in these s-process elements. This is expected, since our targets were specifically selected to have WD companions and a possible history of accretion from an AGB companion.

In the left panel of Figure 6, we see that as expected, there is a positive correlation between the $[\text{Ba}/\text{Fe}]$ and $[\text{Y}/\text{Fe}]$, which strengthens at larger values. The best-fit line obtained using orthogonal distance regression has a slope (0.731 ± 0.055) and intercept (0.166 ± 0.022) dex. While the literature varies in the exact definition of “barium star/dwarf”, most such stars have $[s/\text{Fe}] \gtrsim 0.2 - 0.3$ (where s is an s-process element; D. B. de Castro et al. e.g. 2016; A. Escorza & R. J. De Rosa e.g. 2023;

P. Rekhi et al. e.g. 2024, 2025). In this work, we classify all stars with $[\text{Ba}/\text{Fe}] > 0.25$ as s-process enhanced (i.e. barium dwarfs). For stars which do not have a measured $[\text{Ba}/\text{Fe}]$, we consider $[\text{Y}/\text{Fe}] > 0.35$, based on the linear fit in Figure 6). Under this definition, a total of 40 systems in our sample are classified as s-process enhanced. 4 of these were previously identified by P. Rekhi et al. (2024), who cross-matched the astrometric WD + MS binary catalog to GALAH DR3, while the remaining 36 are new discoveries.

In the right panel of Figure 6, we plot $[\text{Ba}/\text{Y}]$ (i.e. $[\text{Ba}/\text{Fe}] - [\text{Y}/\text{Fe}]$) as a function of the metallicity, $[\text{Fe}/\text{H}]$. This is a measure of the relative abundance of heavy (e.g. Ba, La, Ce) to light s-process (e.g. Y, Zr) elements (often denoted as $[\text{hs}/\text{ls}]$), which is commonly used to compare observations to predicted yields from AGB nucleosynthetic models (e.g. M. Lugaro et al. 2003; D. M. Allen & B. Barbuy 2006). Above $[\text{Fe}/\text{H}] = -1.0$, almost all stars are consistent with negative $[\text{Ba}/\text{Y}]$ within their observational uncertainties, while the three stars with $[\text{Fe}/\text{H}] < -1.0$ have positive $[\text{Ba}/\text{Y}]$. This implies that the yields of the light s-process element, Y, is greater than heavy s-process element, Ba, in AGB donors, unless they are very metal-poor. Although this trend is generally consistent with the literature, we note that there is no clear inverse correlation between the two above $[\text{Fe}/\text{H}] = -1.0$, in contrast to results from previous works (e.g. R. Smiljanic et al. 2007; S. Cristallo et al. 2016; B. Cseh et al. 2018; G. Yang et al. 2024).

In Figure 7, we compare our derived s-process abundances to those from GALAH DR4 (where available). There is an expected correlation between measurements of $[\text{Ba}/\text{Fe}]$ and $[\text{Y}/\text{Fe}]$, with increasing spread at lower

abundances where line strengths are weaker. In the right panel, we compare the [Ba/Y] measurements. There is a subset of systems occupying the upper left corner for which our measured [Ba/Y] are significantly lower than those from GALAH. However, these are not barium dwarfs. Within the sample that overlaps with GALAH, all of the objects we classify as barium dwarfs would also be classified as such based on their GALAH abundances. On the other hand, four objects classified to be barium dwarfs using GALAH are excluded with our abundances.

We find no clear separation in the abundance patterns for systems in the NCE vs. RCE samples, which suggests that – within our sample, which is restricted to RCE stars with relatively small color excesses, low eccentricity, and companion masses near $0.6 M_{\odot}$ – they probe the same underlying population. In particular, there are barium dwarfs in the RCE sample, which would not be expected if they were triples containing tight MS+MS binaries. This reflects the fact that the cut on color excess removes some fraction of true WD + MS binaries from the non-class I sample, as discussed in [N. Yamaguchi et al. \(2025\)](#).

5.2. Dependence on orbital and stellar parameters

In Figure 8, we show the measured [Ba/Fe] against several orbital and stellar parameters: orbital period (P_{orb}), photocenter semi-major axis ($a_0 \times d$, where a_0 is the angular size in mas and d is the distance in kpc; this is equal to the primary semi-major axis for a dark secondary), eccentricity (e), MS star mass (M_1), and companion mass ($M_{2,\text{dark}}$). M_1 was obtained from Gaia’s `binary_masses` catalog. $M_{2,\text{dark}}$ is the mass inferred from the astrometric orbit assuming a completely dark companion, which is a reasonable assumption for a cool WD or NS. To estimate the uncertainty, we use Monte Carlo sampling, generating 100 realizations of $M_{2,\text{dark}}$ by drawing from Gaussian distributions of the input parameters (a_0 , P_{orb} , M_1 , and parallax ϖ) and taking the standard deviation of these realizations. The histogram under each plot shows the fraction of barium dwarfs (as defined in Section 5.1) over the total number of stars in our sample. We selected bins so that the number of systems in each bin is approximately constant. The same plots for [Y/Fe] can be found in Figure 17 in Appendix A.4.

Overall, we see no strong dependence of either [Ba/Fe] or the barium dwarf fraction with orbital period or semi-major axis. There is no strong trend with eccentricity at $e < 0.3$, but at higher eccentricities, we find only one barium star (Section 5.3). This is likely due to highly eccentric systems hosting NS or high-mass WD secon-

daries, which originate from more massive progenitors with lower s-process yields (Section 7).

In panels (D) and (E.2), we see that for barium dwarfs, [Ba/Fe] increases with both increasing primary and secondary mass, consistent with the findings of [P. Rekhi et al. \(2024, 2025\)](#). It is important to point out that these quantities are not independent of each other. More massive primaries require more massive WDs to rule out single MS companions and enter the non-class I sample.

However, the trend with secondary mass eventually falls off for masses above $\sim 0.8 M_{\odot}$. Moreover, across the entire range of companion masses, there are stars which show no s-process enhancement. This suggests that mass is not the sole determining factor for whether or not stars end up as barium dwarfs. We discuss possible physical explanations of the observed trends and scatter in Section 7.

5.3. Ba enhancement in a NS companion?

One barium dwarf is of particular interest (Gaia DR3 source ID 1386979565629462912). It is metal-poor, with $[\text{Fe}/\text{H}] \sim -1.4$, and is strongly barium enhanced, with $[\text{Ba}/\text{Fe}] = 1.33$ dex. The latter is derived from a single Ba II line at 5854 Å, which we have confirmed to be well-fitted by the Gaussian model. Unfortunately, its HIRES spectrum does not contain regions of Y II lines. It is the only barium dwarf in our sample with secondary mass above the Chandrasekhar limit ($1.6 \pm 0.2 M_{\odot}$; Panel (E.1) in Figure 8). It has an orbital period of ~ 870 d and is in a highly eccentric orbit, with $e = 0.76 \pm 0.08$. Additionally, it is classified by [S. Shahaf et al. \(2024\)](#) as an NCE source. These properties all point to a NS companion. However, this would imply a progenitor star with a mass above $\sim 8 M_{\odot}$ which would have evolved into a super-AGB (SAGB) star. The interiors of SAGB stars are thought to have different physical conditions from lower-mass AGB stars, which are expected to affect yields of s-process elements. Theoretical works of SAGB stars generally predict low yields of heavy s-process elements like barium, though model uncertainties associated with mixing processes and nuclear reaction rates can affect precise yields (e.g. [L. Siess 2010](#); [H. H. B. Lau et al. 2011](#); [C. L. Doherty et al. 2017](#)). Additional follow-up spectroscopy with better wavelength coverage to allow measurements of light s-process elements, as well as tracers of neutron density such as rubidium, will allow us to make more robust comparisons with theoretical expectations.

We caution that the Gaia orbit of this source has not yet been validated (e.g. [K. El-Badry et al. 2024d](#)). It is possible that the implied secondary mass is overestimated, meaning that we cannot rule out the possibil-

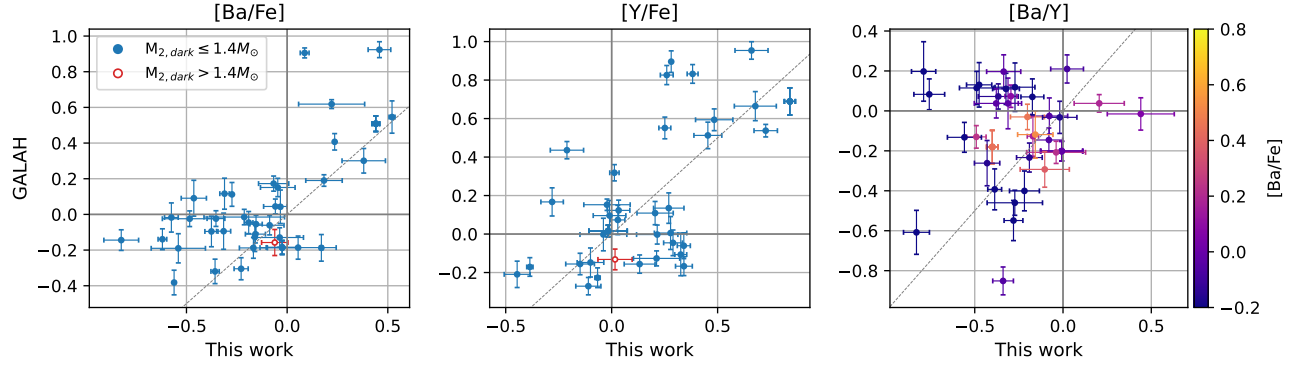


Figure 7. Comparison between our derived Ba and Y abundances, and their differences, against those in the GALAH DR4 catalog. In the rightmost panel, points are colored by [Ba/Fe]. Our abundance measurements are generally correlated with those from GALAH, but many stars are not consistent within their uncertainties. Nevertheless, we agree in almost all cases about whether or not a target is classified as a barium star.

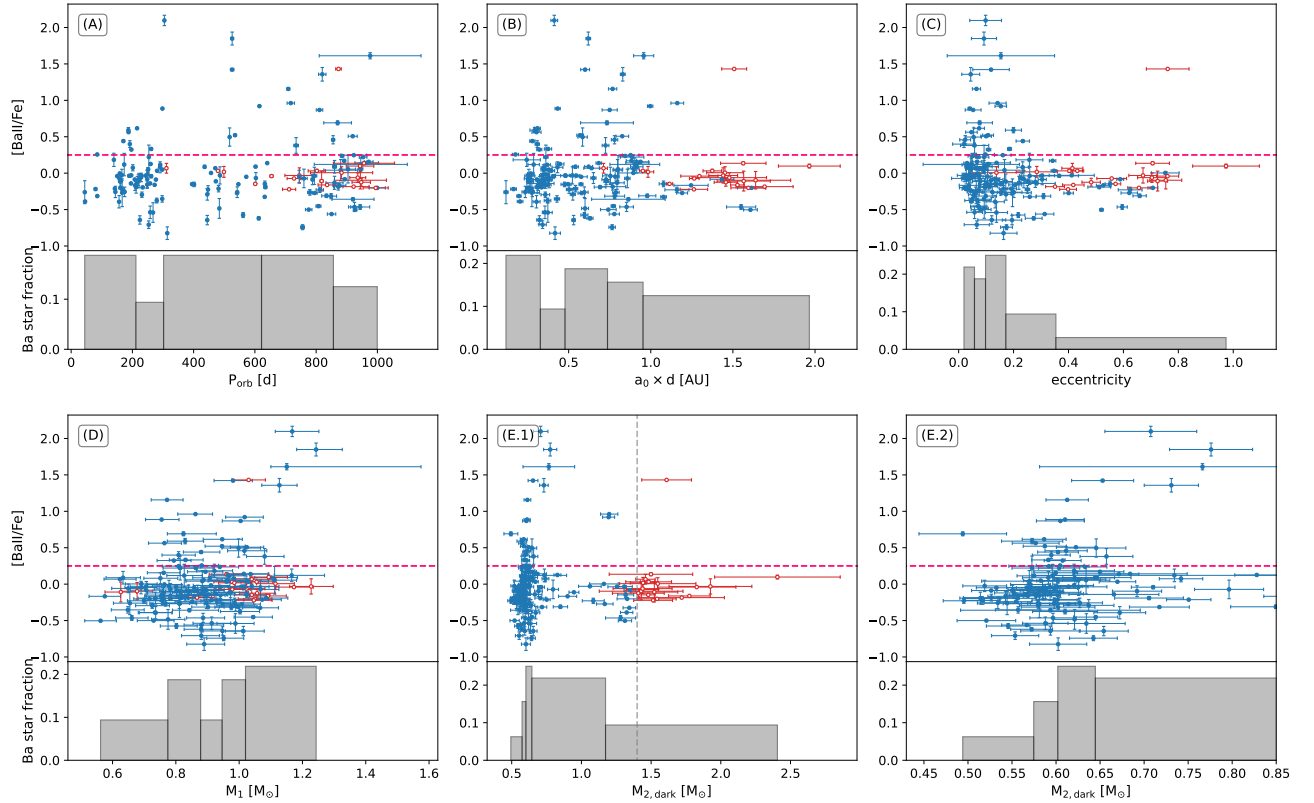


Figure 8. Barium abundance (top) and barium star fraction (bottom) as a function of several orbital and stellar parameters: (A) orbital period, (B) photocenter semi-major axis, (C) eccentricity, (D) primary mass, and (E.1, E.2) dark companion mass. Panel (E.2) is a zoom-in of panel (E.1) for companion masses below $0.85 M_{\odot}$. The pink dashed line indicates the threshold for barium dwarfs, $[\text{Ba}/\text{Fe}] = 0.25$ dex.

ity of a massive WD secondary. We note that primary masses reported in the `binary_masses` table for metal-poor stars tend to be overestimated (K. El-Badry et al. 2024b). Multi-epoch spectroscopic observations to measure and fit RVs will allow us to strengthen constraints on the orbit and nature of the companion.

One other barium dwarf has a notably massive companion (Gaia DR3 source ID 5648541293198448512). However, it has a relatively low implied barium abundance ($[\text{Ba}/\text{Fe}] = 0.26$) and little to no yttrium enhancement, and the large error on its secondary mass makes it consistent with being below the Chandrasekhar limit to within $1 - \sigma$ ($1.5 \pm 0.3 M_{\odot}$). While this makes it a weaker NS candidate with a less robust detection of s-process enhancement, it is in a highly eccentric ($e \sim 0.7$) orbit and may still warrant additional observations.

5.4. Carbon enhanced barium dwarfs

Three barium dwarfs, which are among the most metal-poor in our sample ($[\text{Fe}/\text{H}] \lesssim -1.6$), show deep absorption bands located around $\sim 4300 \text{ \AA}$ that are not predicted by their synthetic spectra (Section 4.2). We show this in the left column of Figure 9. For comparison, we plot the same region for an additional star where this absorption is absent and the synthetic spectrum provides a good fit to the data. This star is similarly metal-poor to the other three ($[\text{Fe}/\text{H}] \sim -2.0$), but is not barium enhanced.

We identify this absorption band as the G band of CH. This, along with the C₂ Swan band (also visible in the spectra of the three stars; see top row of Figure 3), is among the only strong carbon features for metal-poor stars at these effective temperatures and therefore is commonly used in the study of CEMP stars (e.g. A. Goswami et al. 2006; M. Spite et al. 2013; C. J. Hansen et al. 2016; J. E. Norris & D. Yong 2019). In the right column of Figure 9, we over-plot the spectrum of a known CEMP-s star, HE 0441-0652, from Ultraviolet and Visual Echelle Spectrograph (UVES; T. T. Hansen et al. 2016; L. Zhang et al. 2011; ESO proposal number 170.D-0010). The deep absorption of the three barium dwarfs match closely to those of the CEMP-s star. The fact that these features are absent in the star with no barium enhancement supports the idea that the both carbon and s-process elements originate from the same source – a WD companion that was formerly an AGB star. While we leave a more detailed analysis of the carbon abundance for future work, this suggests a smooth transition between the “barium dwarfs” and “CEMP-s” classifications (Section 6).

6. COMPARISON TO LITERATURE BA DWARFS

As discussed in P. Rekhi et al. (2025), the Gaia sample of WD + MS binaries contains barium dwarfs in a region of parameter space that was previously sparsely populated. In Figure 10, we compare several orbital and stellar properties of our systems containing barium dwarfs to those from P. Rekhi et al. (2025). Where available, we also include barium dwarfs and giants from the literature (A. Jorissen et al. 2019; A. Escorza et al. 2019) as well as CEMP-s stars (T. T. Hansen et al. 2016). Since the targets in our work and P. Rekhi et al. (2025) are all selected from the same underlying Gaia sample, on average, they occupy a similar region of the parameter space. However, several additional barium dwarfs from this work extend the tails of the distributions, strengthening previously observed trends and introducing interesting outliers.

In particular, all systems from this work and P. Rekhi et al. (2025) have periods ranging from ~ 100 to 1000 d , which correspond to AU-scale separations, and most have eccentricities between 0 and 0.2. There is a positive relation between the component masses, as the astrometric triage technique requires more massive, and thus luminous, primaries to host more massive WDs (S. Shahaf et al. 2019, 2024). However, as highlighted in Section 5.3, we find two barium dwarfs around massive secondaries very close to or exceeding the Chandrasekhar limit, and these correspond to the two most eccentric systems with $e \sim 0.7$, making them consistent with having NS companions. In addition, there are two barium dwarfs around ultra-massive WD candidates with implied masses $\sim 1.2 M_{\odot}$. It is worth mentioning that these systems have relatively low eccentricities (~ 0.2), consistent with the bulk of the sample and unlike the two NS + MS binary candidates.

There is an inverse trend between the barium abundance and metallicity. This trend is strengthened by the additions from our work, which extends the range of $[\text{Fe}/\text{H}]$ from the P. Rekhi et al. (2025) sample down by more than 1 dex.

Note that while the systems studied this work and P. Rekhi et al. (2024) were selected from the same underlying population from S. Shahaf et al. (2024), P. Rekhi et al. (2024) preferentially selected some targets based on having high eccentricities, and thus the different samples have heterogeneous selection functions. In addition, since the other literature barium dwarfs/stars were not selected based on their AMRFs (Section 2), they are on average more massive and luminous than those of our sample or P. Rekhi et al. (2025).

As described in Section 5.4, we identified evidence of carbon enhancement in a few of the most metal-poor

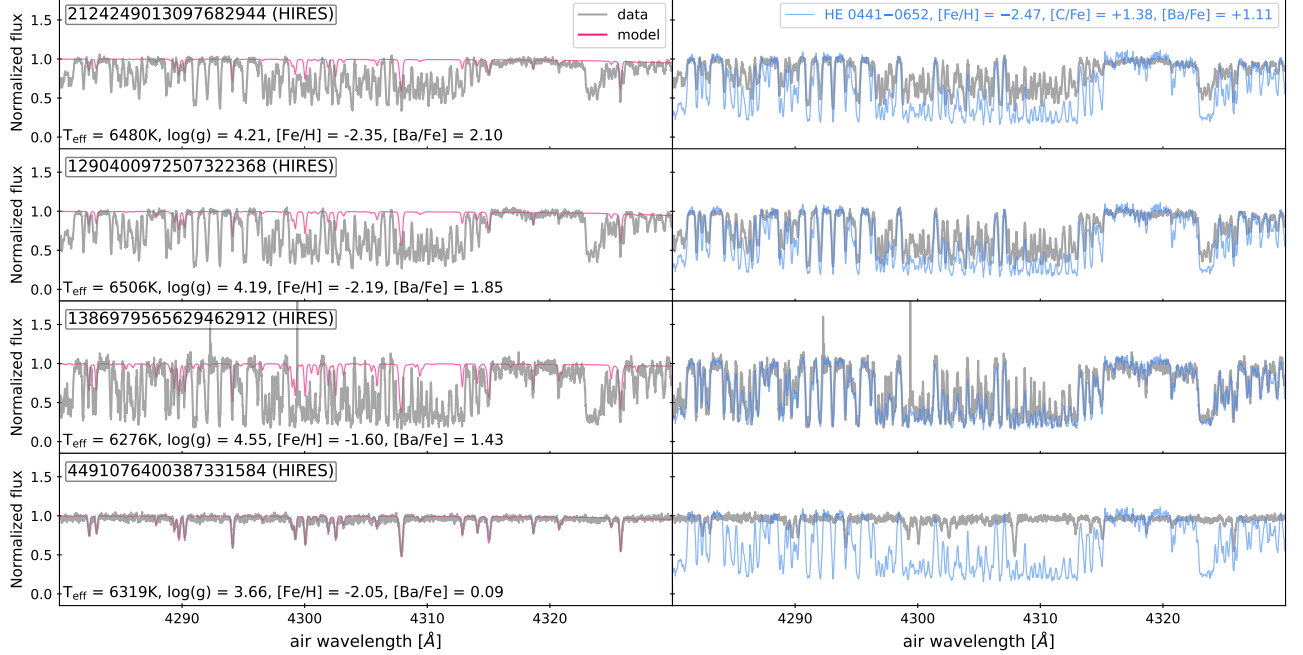


Figure 9. CH G-band region of some of the most metal-poor stars in our sample, all with $[\text{Fe}/\text{H}] \lesssim -1.6$ (gray). The first three stars are barium dwarfs, while the fourth is not. *Left:* In pink, we plot synthetic spectra generated using the best-fit atmospheric parameters corresponding to each star (Section 4.2). *Right:* In blue is the UVES spectrum of a literature CEMP-s star, HE 0441-0652 (T. T. Hansen et al. 2016; L. Zhang et al. 2011). The deep absorption features of the three barium dwarfs are absent in their synthetic spectra and match those of the CEMP-s star, suggesting that they are carbon enhanced. In contrast, there is no evidence of such an enhancement in the fourth star.

barium dwarfs in our sample. Indeed, these overlap in the space of $[\text{Ba}/\text{Fe}]$ vs. $[\text{Fe}/\text{H}]$ with the literature CEMP-s stars. There is no clear dividing line between the two populations, which suggests that they share a common physical origin.

If both barium and carbon indeed originate from an AGB companion, it is natural to ask why carbon enhancement is not present in all barium dwarfs, but only the most metal-poor ones. One possible reason is the higher oxygen abundances in more metal-rich accretors. CEMP-s stars generally have high carbon to oxygen ratios ($[\text{C}/\text{O}] \gtrsim 1$). In the presence of oxygen, carbon binds to it to form carbon monoxide (CO) which, unlike CH or C_2 , does not have strong spectral features in the optical (e.g. D. L. Lambert et al. 1986; T. C. Beers et al. 2007; C. R. Kennedy et al. 2011; Á. Skúladóttir et al. 2015; A. Gonneau et al. 2016). This may explain why CH and C_2 absorption features are only found in the most metal-poor stars, where oxygen abundances are low. This, however, depends on CO molecules surviving in the atmospheres of these stars, which will not be true given high enough effective temperatures. Another possibility is that the accreted material is more carbon-rich at lower metallicities. Indeed, predictions of the carbon abundance, as well as the relative abundance of carbon to oxygen, in theoretical models of AGB stars increases

with decreasing metallicity. This is shown in Section 7 (Figure 12).

7. WHAT DETERMINES S-PROCESS ENHANCEMENT?

In Section 5.2, we studied how the s-process abundances of objects in our sample vary with binary parameters. Here, we discuss the physical origins of the trends, and lack thereof, by comparing to theoretical models of the donor AGB stars (i.e. WD progenitors) and the accreting primaries (i.e. MS stars).

In Figure 11, we plot predicted $[\text{Ba}/\text{Fe}]$ for AGB star envelopes as a function of stellar radius for a range of initial stellar masses and three different metallicities (Z). These predictions are from the FRUITY database (S. Cristallo et al. 2009, 2015, 2016), which provides nucleosynthetic yields and abundances after each dredge-up episode on the AGB, obtained using a modified version of the evolutionary code FRANEC (A. Chieffi & O. Straniero 1989; A. Chieffi et al. 1998; O. Straniero et al. 2006). A complementary database (ph-FRUITY) provides stellar parameters after every thermal pulse, which can be linked to the dredge-up episodes. We show models with $Z = 0.014$ (solar), 0.002, and 0.00024, corresponding to $[\text{Fe}/\text{H}] \sim 0, -0.8$, and -1.8 which roughly spans the metallicities of our observed systems.

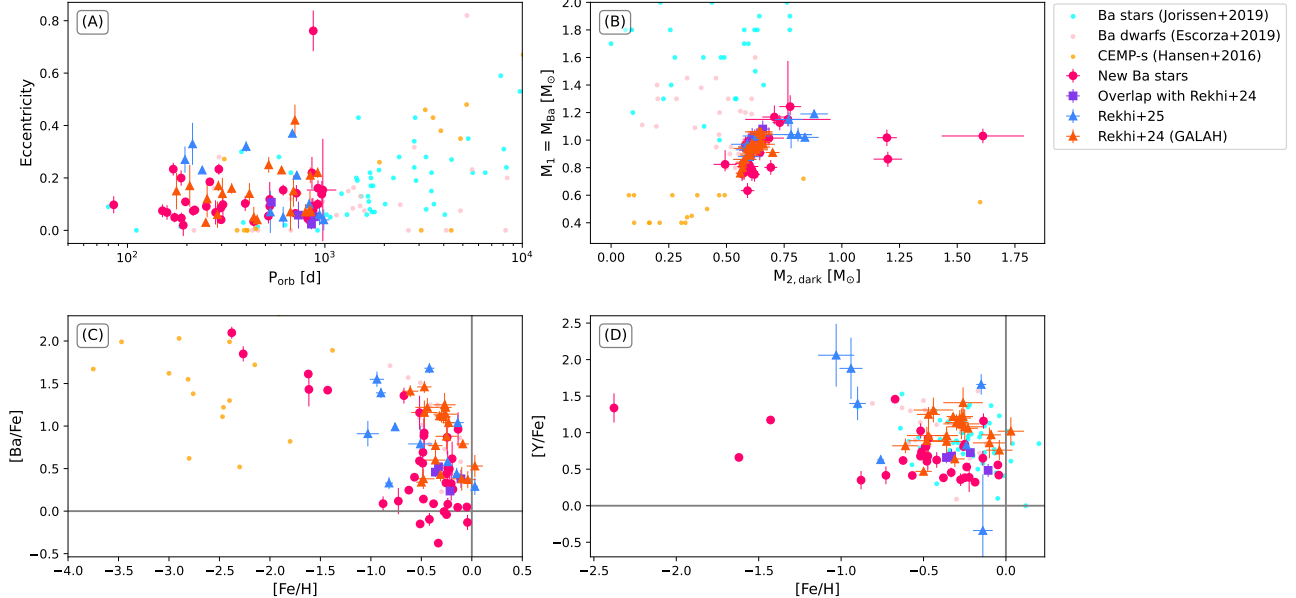


Figure 10. Barium dwarfs from this work and from the published literature, plotted in the space of: (A) eccentricity vs. orbital period, (B) primary vs. secondary mass, (C) $[\text{Ba}/\text{Fe}]$ vs. $[\text{Fe}/\text{H}]$, and (D) $[\text{Y}/\text{Fe}]$ vs. $[\text{Fe}/\text{H}]$. We include the astrometric WD + barium dwarf binaries from P. Rekhi et al. (2025), barium stars/giants and dwarfs with spectroscopic orbits from (A) Jorissen et al. (2019) and A. Escorza et al. (2019) respectively, and CEMP-s stars (T. T. Hansen et al. 2016). Note that for systems with spectroscopic solutions, the secondary mass plotted is the minimum implied mass for an edge-on inclination. The systems from this work and P. Rekhi et al. (2025) reside in a similar region of these plots, but our additions extend the tails of the distributions. In particular, the most metal-poor systems in our sample bridge the gap between normal barium dwarfs and metal-poor CEMP-s stars.

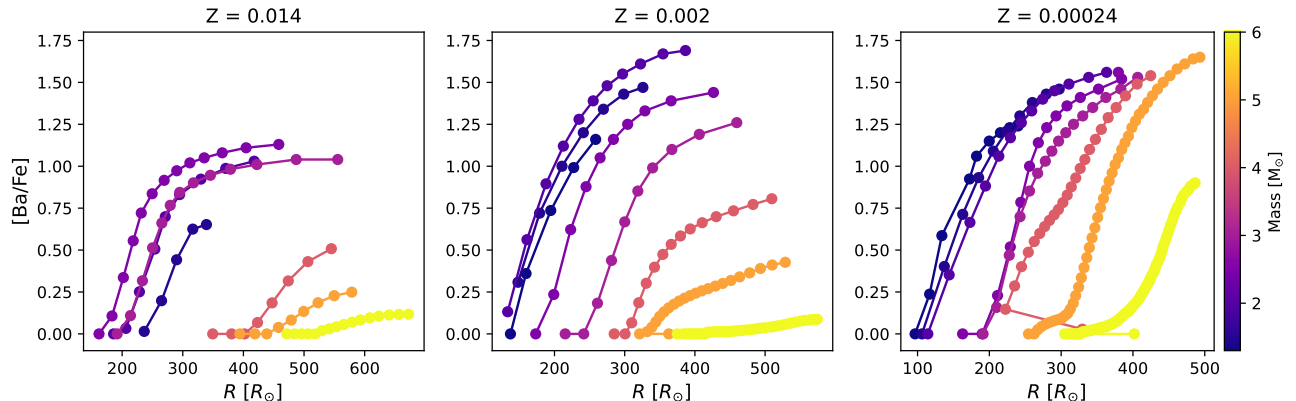


Figure 11. Predicted barium abundance of AGB star envelopes as a function of radius from the FRUITY models. We show models for initial masses ranging from 1.3 to $6.0 M_{\odot}$ at three different metallicities. At a fixed radius, the barium yield generally falls with increasing mass and metallicity.

$[\text{Ba}/\text{Fe}]$ is predicted to increase as the AGB star evolves and its maximum radius grows. Thus, the expected enhancement in the accretor due to MT from an AGB donor depends on when MT occurs. Therefore, we may expect a correlation between measured $[\text{Ba}/\text{Fe}]$ of the MS stars and the binaries' *initial* separations. However, this evidently does not translate to a strong correlation with the present-day separations (Section 5.2;

Figure 8). This is not unexpected, as MT can change the orbital separation in ways that may depend non-trivially on the binary parameters (see Section 7.1 for further discussion).

The predicted $[\text{Ba}/\text{Fe}]$ also varies with Z . For stars of all masses, $[\text{Ba}/\text{Fe}]$ generally increases with decreasing Z at a fixed radius. This partially explains the trend between the observed s-process abundances of our bar-

ium dwarfs with their metallicities (Section 5.1; Figure 5). For masses between ~ 2.0 and $4.0 M_{\odot}$, the trend is broken at early times (i.e. at smaller radii), which may add scatter to the observed trend.

We can similarly study the evolution of $[\text{Ba}/\text{Y}]$ as a function of mass and metallicity in the FRUITY models. Overall, this evolution is more complex than that of $[\text{Ba}/\text{Fe}]$. It is generally positive for masses below $\sim 4 M_{\odot}$ and $Z \lesssim 0.014$. For more massive stars, $[\text{Ba}/\text{Y}]$ evolves non-monotonically, starting at small positive values, then dropping to negative values before increasing again.

Additionally, in the left panel of Figure 12, we plot the predicted $[\text{C}/\text{H}]$ ($= [\text{C}/\text{Fe}] - [\text{Fe}/\text{H}] \approx [\text{C}/\text{Fe}] - \log_{10}(Z)$) as a function of stellar radius and metallicity for a fixed initial mass of $2 M_{\odot}$. $[\text{C}/\text{H}]$ generally increases with decreasing metallicity, which we may expect to result in more carbon-rich accretors in metal-poor systems. In the right panel, we plot the predicted $[\text{C}/\text{O}]$ which similarly shows an anti-correlation with metallicity, though more pronounced throughout the AGB evolution. If the carbon is indeed effectively locked up in carbon monoxide, this may be another important explanation for the CEMP stars (Section 6).

Besides the chemical composition of the accreted material, the present-day abundances will also depend on the amount of dilution experienced by this material as a result of mixing in the convective envelope of the accretor. To investigate this, we use the 1D stellar evolution code Modules for Experiments in Stellar Astrophysics (MESA, version r24.03.1; B. Paxton et al. 2011, 2013, 2015, 2018, 2019; A. S. Jermyn et al. 2023) to produce MS star models and study changes in the masses of their convective envelopes as a function of the total stellar mass and metallicity. We take the model closest to when the core mass fraction of H reaches 30%. Our grid covers a mass range from 0.6 to $1.2 M_{\odot}$ to span the range of MS star masses in our sample, and we test the same metallicities as the chosen FRUITY models. We plot the results in Figure 13. We see that the mass in the convective envelope decreases steeply with both stellar mass and Z . At solar metallicity, the mass in the convective envelope becomes negligible above $\sim 1.2 M_{\odot}$, while at $Z = 0.002$ and 0.00024 , this occurs by $\sim 0.9 M_{\odot}$. This means that equal amounts of accreted material with the same s-process content will likely lead to stronger enhancement in a more massive and more metal-poor star.

7.1. Population modeling of Ba dwarf binaries

Here, we take the theoretical models described above to predict barium abundances in the population of astrometric WD + MS binaries to test whether or not the

aforementioned factors are able to account for the observed spread.

We build on the results of N. Yamaguchi et al. (2025), who used a forward modeling approach to create a mock non-class I sample with properties that closely approximate the true S. Shahaf et al. (2024) sample. They start with a simulated population of Galactic zero-age binaries, then model the stellar evolution of each component as well as their orbital evolution due to binary interactions to obtain the present-day population of WD + MS binaries. In their fiducial model, the change in orbital separation due to MT from AGB donors for systems with initial accretor-to-donor mass ratios exceeding ~ 0.4 – which ultimately become the AU-scale WD + MS binaries that we study in this work – is calculated using the relations derived by G. E. Soberman et al. (1997) for fully non-conservative MT (i.e. $\beta = 1$). Epoch astrometry is predicted for each present-day binary based on the Gaia scanning law which is then fit with astrometric models. A subset of these orbital solutions form the catalog of astrometric binaries which reproduces the key features of the true catalog published in Gaia DR3, suggesting that the selection function derived by this method is reasonable (K. El-Badry et al. 2024a). Finally, as done by S. Shahaf et al. (2024), non-class I systems are selected based on the AMRF. We refer readers to N. Yamaguchi et al. (2025) for an in-depth description of this process.

For each WD + MS binary in the mock non-class I sample, we know the initial (i.e. pre-MT) stellar and orbital parameters. From the metallicity of the system, mass of the AGB donor (i.e. the WD progenitor), and initial Roche lobe radius, we can interpolate the FRUITY models (Figure 11) to predict the barium abundance in the donor at the onset of MT, $[\text{Ba}/\text{Fe}]_{\text{AGB}}$ which is accreted onto the companion. We estimate the mass of the companion’s convective envelope, M_{conv} , by interpolating our MESA models (Figure 13) at the companion mass and metallicity.

Assuming efficient mixing, the final abundance in the accretor’s convective envelope, $[\text{Ba}/\text{Fe}]_f$, is given by:

$$\log_{10} \left(\frac{10^{[\text{Ba}/\text{Fe}]_i} M_{\text{conv}} + 10^{[\text{Ba}/\text{Fe}]_{\text{AGB}}} M_{\text{acc}}}{M_{\text{conv}} + M_{\text{acc}}} \right) \quad (2)$$

where $[\text{Ba}/\text{Fe}]_i$ is the initial barium abundance in the MS companion before MT and M_{acc} is the mass of material accreted. This assumes that both components have the same iron abundance, which is reasonable. Since the accretors in our systems have not left the MS, we assume no initial barium enhancement, $[\text{Ba}/\text{Fe}]_i = 0$. By default, M_{acc} is taken to be 1% of the AGB donor’s envelope (i.e. donor mass - WD mass) which corresponds, on

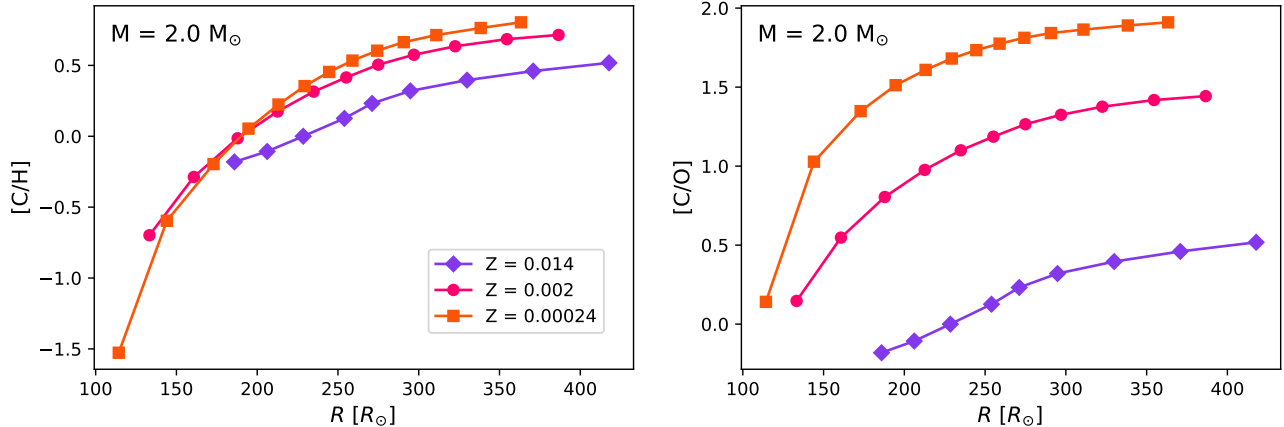


Figure 12. Evolution of [C/H] (Left) and [C/O] (Right) for an initially $2 M_{\odot}$ star as predicted by FRUITY models with a range of metallicities. [C/H], which represents the total carbon yield, increases modestly with decreasing metallicity at fixed radius, but [C/O] increases by almost two dex.

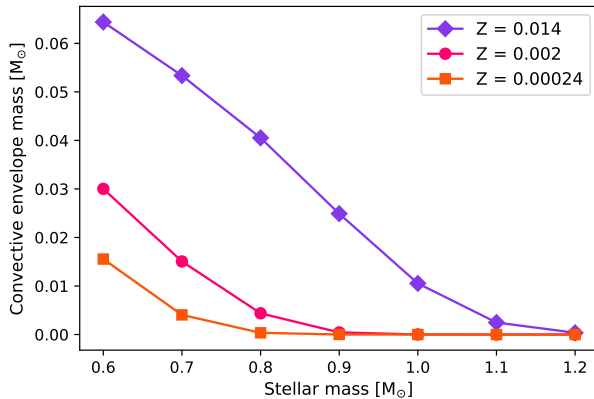


Figure 13. Mass in the convective envelope predicted by MESA models at different metallicities. The convective envelope shrinks with increasing stellar mass and decreasing metallicity. This means that s-process rich material from an AGB donor will experience less dilution, and therefore lead to a stronger surface s-process enhancement, in more massive and metal-poor accretors.

average, to $\sim 0.015 M_{\odot}$, but we experiment with the effects of varying the efficiency of mass transfer. Note that while this calculation is inconsistent with the fully non-conservative assumption made in generating the simulated population, the resulting discrepancy is minimal for such small amounts of accreted material.

In the top of row of Figure 14, we plot the predicted $[\text{Ba}/\text{Fe}]_f$ as a function of several orbital and stellar parameters for the simulated sample using the fiducial model of orbital evolution adopted by N. Yamaguchi et al. (2025). In total, fewer than 10% of the simulated MS stars have $[\text{Ba}/\text{Fe}]_i > 0.25$ dex. This fraction is primarily determined by the assumed initial separations of the binaries. As shown in Figure 11, $[\text{Ba}/\text{Fe}]$ increases rapidly with the radius/age of the AGB donor.

In the fiducial model, systems with initial Roche lobe radii $\lesssim 200 R_{\odot}$ comprise the bulk of those that end up as AU-scale WD + MS binaries with $P_{\text{orb}} < 1000$ d and thus enter our sample. AGB stars at these radii are in very early phases of s-process nucleosynthesis, and thus the accreted material is not yet strongly enriched in barium.

Conversely, if we adopt a different model such that systems with initially wider orbits experience more orbital shrinkage to form the AU-scale systems, MT would have begun when the AGB donors were more evolved, resulting in a larger fraction of barium dwarfs. As one example, if we continue to assume fully non-conservative MT but with some mass loss via wind from the donor ($A = 5, \alpha = 0.2, \beta = 0.8$; G. E. Soberman et al. 1997), our systems would have experienced MT from AGB donors with radii as large as $\sim 400 R_{\odot}$. This increases the predicted fraction of barium dwarfs to $\sim 30\%$. We show the results of this model in the bottom row of Figure 14. Although the relation between initial to final separation is not one-to-one, there is a general trend of $[\text{Ba}/\text{Fe}]_f$ with the orbital period in the simulation, with a smaller fraction of barium dwarfs below ~ 1 yr. We do not find evidence of such a trend in our observed systems (Figure 8). This likely reflects the fact that the true orbital evolution is more diverse and complex than assumed by our model, meaning there is more scatter in the relation between initial and final separations. Additionally, most classical barium stars/dwarfs are at periods > 1000 d, so the fraction may still increase at longer periods.

In the bottom row, $[\text{Ba}/\text{Fe}]_f$ generally rises with increasing component masses and decreasing metallicity. This is primarily the effect of dilution, combined with the correlation between the component masses for sys-

tems that enter the non-class I sample and the dependence of predicted yields on these parameters. We see qualitatively similar trends in our observed systems (Figure 8). However, the same trends are absent or weaker for the results plotted in the top row. One reason is that more massive accretors are on average accompanied by more massive AGB donors, and in the fiducial model, the vast majority of donors with masses $\gtrsim 2 M_{\odot}$ (around MS companions with masses $\gtrsim 0.8 M_{\odot}$) interact prior to significant s-process element production ($\lesssim 200 R_{\odot}$). This counteracts the effect of dilution.

The effect of dilution is strengthened as the mass of material accreted becomes comparable to the mass of the accretor's convective envelope. Therefore, if we instead assume that only 0.5% of the mass lost by the AGB donor is accreted by the companion (corresponding to $\sim 0.008 M_{\odot}$), the trends of $[\text{Ba}/\text{Fe}]_f$ with component masses and metallicity – which are driven by dilution – become stronger. As expected, the total fraction of barium dwarfs decreases. Conversely, if the fraction accreted is increased to 10%, these trends weaken as $M_{\text{acc}} \sim 0.15 M_{\odot} \gg M_{\text{conv}}$. There is a modest increase in the fraction of barium dwarfs by 5-10% from the default assumption of 1%, depending on the model. However, the magnitude of barium enhancement rises more significantly, with more than double the number of stars having $[\text{Ba}/\text{Fe}] > 1.0$.

We do not attempt to further refine our simulation to reproduce the exact features of the observed systems and their measured s-process abundances. For this, we must consider the selection of our targets from the non-class I systems which is not homogeneous across the multiple observing programs. Moreover, there exists degeneracies in the orbital evolution predicted by the [G. E. Soberman et al. \(1997\)](#) relation for different choices of parameters which are difficult to disentangle. In addition, for simplicity, we only considered dilution in the context of the outermost convective envelope. However, in reality, non-convective mixing processes such as thermohaline mixing and atomic diffusion (e.g. [J. Sevilla et al. 2022](#); [A. Behmard et al. 2023](#)) may have non-negligible effects, particularly as the convective layer becomes very thin at larger stellar masses and lower metallicities. It is also worth mentioning that the $[\text{Ba}/\text{Fe}]_i = 0$ assumption is a simplification as it has been shown to depend on $[\text{Fe}/\text{H}]$ (e.g. [P. E. Nissen & W. J. Schuster 2011](#); [H. Reggiani et al. 2017](#); [A. M. Amarsi et al. 2020](#)). However, we have confirmed that such a variation only reduces the total

fraction of barium dwarfs in our simulated population by a few percent⁸.

This exercise suggests that a key factor in determining whether or not a star that has accreted material from an AGB donor becomes a barium dwarf is how evolved the donor was when interaction began. This is in turn determined by the initial separation of the binary. Dilution plays a minor role for systems in our sample, most of which contain MS stars with thin convective envelopes. As a result, the observed barium abundances do not place strong constraints on the MT efficiency. Overall, in the framework of this model, it is not surprising that many AU-scale WD + MS binaries are *not* enhanced in barium, simply because they interacted relatively early on the AGB. This may at least partially explain the fact that most previously discovered barium stars and related systems are in wider orbits than those of our sample (Figure 10). For the same reason, we may expect a larger fraction of barium dwarfs to be discovered in future Gaia data releases, which will be sensitive to binaries with longer orbital periods.

8. CONCLUSIONS

We obtained high-resolution optical spectroscopy for 178 WD + MS binary candidates selected from the Gaia DR3 catalog of astrometric binaries. These systems have orbital periods of $\sim 100 - 1000$ d, corresponding to AU-scale separations, and are thought to be products of MT from AGB donors. However, the exact nature of the MT process remains uncertain. Through spectral analysis, we constrained stellar parameters of the MS companions and derived chemical abundances, focusing on the s-process elements barium and yttrium. We summarize our key findings below:

- We selected targets from the [S. Shahaf et al. \(2024\)](#) sample of systems classified as likely WD + MS binaries based on their Gaia astrometric orbits. We specifically selected several metal-poor targets with $[\text{Fe}/\text{H}] < -1.0$ (Section 2, Figure 1).
- We use ionization/excitation equilibrium of iron lines to determine T_{eff} , $\log(g)$, $[\text{Fe}/\text{H}]$, and ξ . We find general agreement with existing literature values (Section 4.1, Figure 2).
- We measure abundances of iron (Fe I, Fe II), α -elements (Mg I, Ca I, Si I), and s-process elements (Ba II, Y II) (Section 4.3, Figure 5). We identify

⁸ We tested a linear fit to data from [H. Reggiani et al. \(2017\)](#) and [P. E. Nissen & W. J. Schuster \(2011\)](#): $[\text{Ba}/\text{Fe}] = -0.08625[\text{Fe}/\text{H}] - 0.14492$.

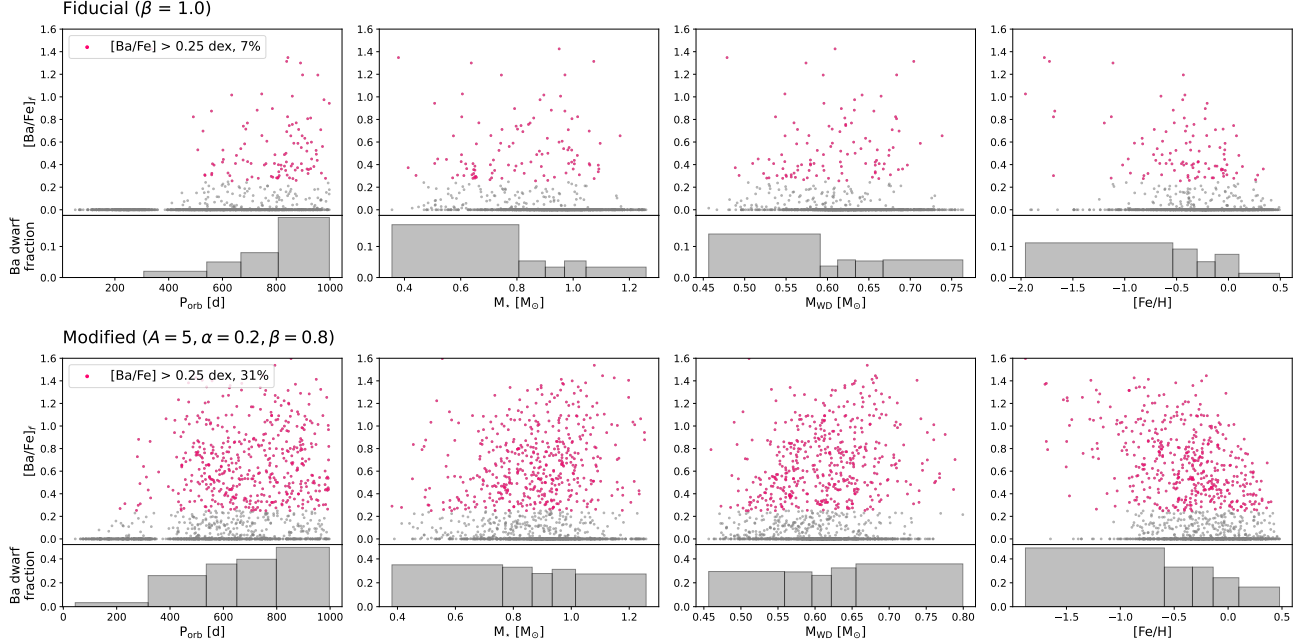


Figure 14. Predicted barium abundance and barium dwarf fraction as a function of several orbital and stellar parameters for the simulated non-class I sample. For visual clarity, we plot a subset of 1500 systems. In magenta, we highlight the barium dwarfs, with $[\text{Ba/Fe}] > 0.25 \text{ dex}$. In the top row are results using the fiducial model of orbital evolution via MT adopted by N. Yamaguchi et al. (2025), using relations from G. E. Soberman et al. (1997) with $\beta = 1$ (i.e. fully non-conservative MT with mass loss via isotropic re-emission from the accretor). In the bottom row are results using the same relations, but with non-zero α (i.e. still fully non-conservative, but with some mass loss via winds from the donor). On average, the latter results in more orbital shrinkage, so that systems with initially wider separations and correspondingly more evolved AGB donors enter our sample. As s-process yields increase with time on the AGB, this leads to a larger fraction of barium dwarfs.

40 barium dwarfs ($[\text{Ba/Fe}] > 0.25 \text{ dex}$ OR $[\text{Y/Fe}] > 0.35 \text{ dex}$), 36 of which are new discoveries (Section 5.1).

- About 25% of the likely WD+MS binaries in our sample are enriched in s-process elements. Their s-process abundances are uncorrelated with orbital period, in agreement with previous work. The incidence of s-process enhancement drops at high eccentricities and companion masses above $1.4 M_{\odot}$, likely reflecting the presence of NS rather than WD companions. At lower companion masses, we find weak positive correlations with the component masses and an inverse correlation with the iron abundance (Section 5.2, Figure 8).
- We identify two barium dwarfs around companions whose masses may exceed the Chandrasekhar limit and which are in highly eccentric ($e > 0.7$) orbits, making them possible MS + NS binaries. Further high-resolution spectroscopy with increased wavelength coverage containing additional s-process lines is necessary to strengthen constraints on their abundances, and multi-epoch radial velocities are needed to validate their orbits and confirm their nature (Section 5.3).

- We find evidence of strong C enhancement in three out of four of the most metal-poor barium dwarfs with $[\text{Fe/H}] < -1.5$ (Figure 9), suggesting that there exists a smooth transition between barium dwarfs and CEMP-s stars (Section 5.4).
- Our sample roughly doubles the current number of barium dwarfs in AU-scale orbits. It extends the observed trend of $[\text{Ba/Fe}]$ with $[\text{Fe/H}]$ by P. Rekhi et al. (2025) to significantly more metal-poor stars with $[\text{Fe/H}] < -2.0 \text{ dex}$. (Section 6, Figure 10)
- Using theoretical AGB nucleosynthetic yields from the FRUITY database and 1D models of the companion MS stars to predict barium abundances in a simulated population of WD + MS binaries, we show that the observed diversity of s-process abundances can be attributed to the range in metallicities and component masses (which affect both the AGB yields and mass in the accretor's convective envelope) and the age of the AGB donor at interaction. We also find that the fraction of stars that are barium dwarfs is sensitive to the assumed orbital evolution via MT. In general, systems for which MT began at initially wide separations with

evolved AGB donors end up with greater barium enhancements (Section 7, Figure 14).

Future data releases from the Gaia mission will build on this sample, extending to longer orbital periods and allowing for a more homogeneous selection of these systems to conduct more complete and detailed population-level studies.

ACKNOWLEDGMENTS

We thank Ana Escorza, Sophie van Eck, Alain Jorissen, and Param Rekhi for useful conversations. We are grateful to Yuri Beletsky, Sam Kim, Angela Hempel, and Maren Hempel for observing help. This research benefited from discussions in the ZTF Theory Network, funded in part by the Gordon and Betty Moore Foundation through Grant GBMF5076. NY acknowledges support from the Ezoe Memorial Recruit Foundation scholarship. This research was supported by NSF grant AST-2307232.

AUTHOR CONTRIBUTIONS

NY was responsible for completing the data analysis and population modeling of the systems in this work as well as writing and submitting the manuscript. KE advised NY throughout the project, from initial conceptualization to editing the manuscript. HR provided expertise on the spectral analysis and ensured that the stellar parameters and abundances obtained were reliable. RA re-analyzed Gaia XP spectra using corrected parallaxes appropriate for our systems, which we used in our analysis. SS created the original sample of astrometric binaries from which our systems were selected.

Facilities: Max Planck:2.2m (FEROS), Magellan:Clay (MIKE), Keck:I (HIRES)

Software: RRevIEW (<https://github.com/madeleine-mckenzie/RRevIEW>), q2 (<https://github.com/astroChasqui/q2>), iSpec (<https://www.blancocuaresma.com/s/iSpec/manual/introduction>), gaiamock (<https://github.com/kareemelbadry/gaiamock>)

APPENDIX

A. APPENDIX INFORMATION

A.1. *Results of stellar parameter determination*

In Figure 15, we show examples of the final output from q2 in measuring stellar parameters via excitation/ionization equilibrium for three targets with varying degrees of success (Section 4.1). Successful convergence is achieved when there are minimal trends in the implied abundances of both FeI and FeII as a function of several line properties, plotted in each of the three rows. Having a small number of lines with reliably measured EWs as a result of poor SNR and/or rotational broadening can lead to convergence failure. For a typical spectrum of our sample, we find that our method is effective for $v \sin(i) \lesssim 20$ km/s. Detailed descriptions for the three examples can be found in the figure caption.

A.2. *Effect of systematic uncertainty on T_{eff}*

As discussed in Section 4.1, the best-fit T_{eff} values derived from high-resolution spectra deviate from those of R. Andrae et al. (2023) which are measured using Gaia XP spectra and broad-band photometry. In most cases, the SEDs predicted using T_{eff} values from the latter are more consistent with photometric observations. Nevertheless, we use the spectroscopic stellar parameters to derive our fiducial abundances. Here, we re-derive them using T_{eff} values from R. Andrae et al. (2023), and in Figure 16, we compare the resulting [Ba/H] (as opposed to [Ba/Fe] which also depends on the iron abundance). We find that our measurements are generally higher, and that this discrepancy increases for cooler stars. However, the discrepancy is less than 0.3 dex for the bulk of the sample. Using T_{eff} values from R. Andrae et al. (2023) would only reduce the total number of stars classified to be barium dwarfs by one (Gaia DR3 source ID 3474329544020730496, with a [Ba/Fe] close to the lower bound of 0.25 dex).

A.3. *Tables of atmospheric parameters and abundances*

In Tables 2 and 3, we provide snippets of tables summarizing the derived atmospheric parameters and abundances. The full tables containing information for all 160 stars in our final sample can be downloaded from the online journal.

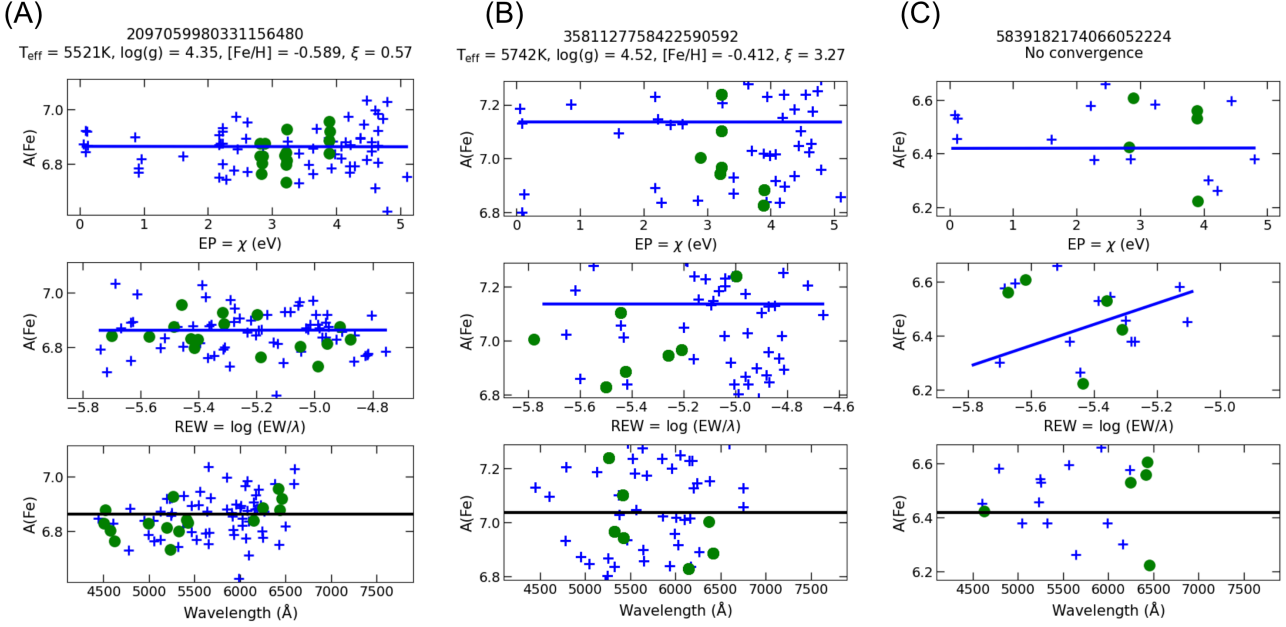


Figure 15. Results of attempting to achieve excitation/ionization equilibrium using iron lines with q2 (Section 4.1). The blue cross markers correspond to Fe I, while the green circle markers correspond to Fe II lines. The best fit linear model is also plotted in each panel. We show an example of a spectrum which (A) achieves convergence with reliable results on the first attempt, (B) requires fixing $\log(g)$ to its initial value to avoid it from going to 5.0, and (C) fails to achieve convergence due to rotationally broadened lines. Note that the scatter in the data depends on the SNR and resolution of each spectrum.

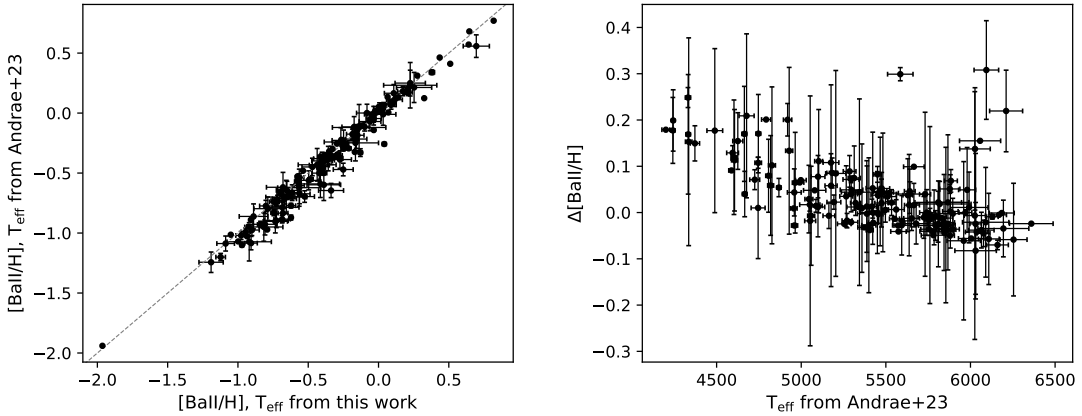


Figure 16. *Left:* Comparison of barium abundances derived taking the best-fit T_{eff} from this work vs. the value from R. Andrae et al. (2023) (modified to use parallaxes corrected for binary motion; Section 4.1). We take our best-fit values for all other stellar parameters ($[\text{Fe}/\text{H}]$, $\log(g)$, and ξ). *Right:* The difference in the abundances as a function of T_{eff} . The difference increases for cooler stars, where the two T_{eff} values become increasingly discrepant.

A.4. Trends with yttrium abundance

Figure 17 plots $[\text{Y}/\text{Fe}]$ as a function of several orbital and stellar parameters, analogous to that of $[\text{Ba}/\text{Fe}]$ in Figure 8 where similar trends (or lack thereof) are found (Section 5.2).

REFERENCES

Abate, C., Pols, O. R., & Stancliffe, R. J. 2018, A&A, 620, A63, doi: [10.1051/0004-6361/201833780](https://doi.org/10.1051/0004-6361/201833780)

Abate, C., Pols, O. R., Stancliffe, R. J., et al. 2015, A&A, 581, A62, doi: [10.1051/0004-6361/201526200](https://doi.org/10.1051/0004-6361/201526200)

Gaia DR3 source ID	Instrument	T_{eff} [K]	$\log(g)$	ξ [km s $^{-1}$]	[Fe/H]
2808994137268673152	HIRESb	6064 ± 307	4.80 ± 0.76	2.71 ± 1.61	-0.29 ± 0.22
2124249013097682944	HIRESb	6480 ± 183	4.21 ± 0.31	1.02 ± 0.14	-2.35 ± 0.13
2097059980331156480	HIRESb	5521 ± 43	4.35 ± 0.11	0.57 ± 0.12	-0.59 ± 0.03
2795884385252655232	HIRESb	6250 ± 307	4.57 ± 0.47	0.24 ± 1.16	-0.66 ± 0.17
2105234402606388352	HIRESb	5309 ± 32	4.27 ± 0.08	0.18 ± 0.33	-0.78 ± 0.03
...					

Table 2. Atmospheric parameters for systems which achieved successful convergence (Section 4.1). The complete table can be downloaded online.

Gaia DR3 source ID	$A(\text{Fe I})$	$N(\text{Fe I})$	$A(\text{Fe II})$	$N(\text{Fe II})$	$A(\text{Ba II})$	$N(\text{Ba II})$	$A(\text{Y II})$...
2808994137268673152	7.17 ± 0.03	31	7.04 ± 0.05	12	2.10 ± 0.09	2	1.89 ± 0.20	
2124249013097682944	5.08 ± 0.02	75	5.06 ± 0.07	6	2.02 ± 0.07	2	1.20 ± 0.20	
2097059980331156480	6.87 ± 0.01	63	6.84 ± 0.02	17	1.47 ± 0.04	2	1.50 ± 0.04	...
2795884385252655232	6.79 ± 0.02	20	6.76 ± 0.04	10	2.97 ± 0.09	2	3.01 ± 0.02	
2105234402606388352	6.68 ± 0.01	60	6.66 ± 0.02	14	1.38 ± 0.10	2	1.29 ± 0.01	
...								

Table 3. Absolute abundances derived for systems in Table 2 (Section 4.3). The reported errors are the standard deviations of abundances inferred from multiple lines divided by square root of the number of lines (N). In the case of a single line, we adopt a fixed error of 0.2 dex. The complete table can be downloaded online.

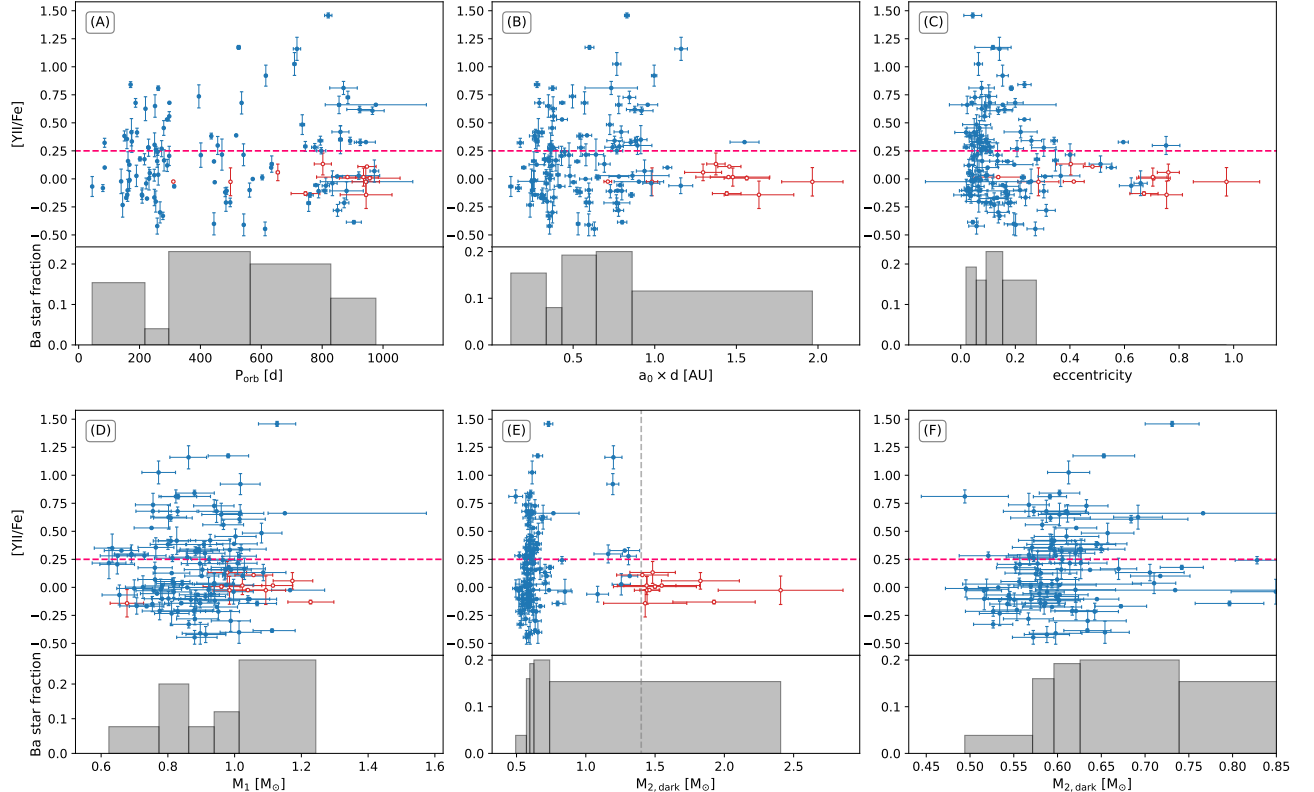


Figure 17. Analogous to Figure 8, but plotting [Y/Fe] instead of [Ba/Fe].

Adibekyan, V. Z., Delgado Mena, E., Sousa, S. G., et al. 2012, *A&A*, 547, A36, doi: [10.1051/0004-6361/201220167](https://doi.org/10.1051/0004-6361/201220167)

Allen, D. M., & Barbuy, B. 2006, *A&A*, 454, 917, doi: [10.1051/0004-6361:20064968](https://doi.org/10.1051/0004-6361:20064968)

Amarsi, A. M., Lind, K., Osorio, Y., et al. 2020, *A&A*, 642, A62, doi: [10.1051/0004-6361/202038650](https://doi.org/10.1051/0004-6361/202038650)

Andrae, R., Rix, H.-W., & Chandra, V. 2023, *ApJS*, 267, 8, doi: [10.3847/1538-4365/acd53e](https://doi.org/10.3847/1538-4365/acd53e)

Aoki, W., Beers, T. C., Christlieb, N., et al. 2007a, *ApJ*, 655, 492, doi: [10.1086/509817](https://doi.org/10.1086/509817)

Aoki, W., Beers, T. C., Christlieb, N., et al. 2007b, *ApJ*, 655, 492, doi: [10.1086/509817](https://doi.org/10.1086/509817)

Arentsen, A., Placco, V. M., Lee, Y. S., et al. 2022, *MNRAS*, 515, 4082, doi: [10.1093/mnras/stac2062](https://doi.org/10.1093/mnras/stac2062)

Asplund, M., Amarsi, A. M., & Grevesse, N. 2021, *A&A*, 653, A141, doi: [10.1051/0004-6361/202140445](https://doi.org/10.1051/0004-6361/202140445)

Beers, T. C., & Christlieb, N. 2005, *ARA&A*, 43, 531, doi: [10.1146/annurev.astro.42.053102.134057](https://doi.org/10.1146/annurev.astro.42.053102.134057)

Beers, T. C., Sivarani, T., Marsteller, B., et al. 2007, *AJ*, 133, 1193, doi: [10.1086/511183](https://doi.org/10.1086/511183)

Behmard, A., Sevilla, J., & Fuller, J. 2023, *MNRAS*, 518, 5465, doi: [10.1093/mnras/stac3435](https://doi.org/10.1093/mnras/stac3435)

Belloni, D., Zorotovic, M., Schreiber, M. R., et al. 2024, *A&A*, 686, A61, doi: [10.1051/0004-6361/202449235](https://doi.org/10.1051/0004-6361/202449235)

Bernstein, R., Shectman, S. A., Gunnels, S. M., Mochnacki, S., & Athey, A. E. 2003, in Society of Photo-Optical Instrumentation Engineers (SPIE) Conference Series, Vol. 4841, Instrument Design and Performance for Optical/Infrared Ground-based Telescopes, ed. M. Iye & A. F. M. Moorwood, 1694–1704, doi: [10.1117/12.461502](https://doi.org/10.1117/12.461502)

Blanco-Cuaresma, S. 2019, *MNRAS*, 486, 2075, doi: [10.1093/mnras/stz549](https://doi.org/10.1093/mnras/stz549)

Blanco-Cuaresma, S., Soubiran, C., Heiter, U., & Jofré, P. 2014, *A&A*, 569, A111, doi: [10.1051/0004-6361/201423945](https://doi.org/10.1051/0004-6361/201423945)

Brahm, R., Jordán, A., & Espinoza, N. 2017, *PASP*, 129, 034002, doi: [10.1088/1538-3873/aa5455](https://doi.org/10.1088/1538-3873/aa5455)

Buder, S., Sharma, S., Kos, J., et al. 2021, *MNRAS*, 506, 150, doi: [10.1093/mnras/stab1242](https://doi.org/10.1093/mnras/stab1242)

Buder, S., Kos, J., Wang, X. E., et al. 2025, *PASA*, 42, e051, doi: [10.1017/pasa.2025.26](https://doi.org/10.1017/pasa.2025.26)

Cayrel, R., Depagne, E., Spite, M., et al. 2004, *A&A*, 416, 1117, doi: [10.1051/0004-6361:20034074](https://doi.org/10.1051/0004-6361:20034074)

Chieffi, A., Limongi, M., & Straniero, O. 1998, *ApJ*, 502, 737, doi: [10.1086/305921](https://doi.org/10.1086/305921)

Chieffi, A., & Straniero, O. 1989, *ApJS*, 71, 47, doi: [10.1086/191364](https://doi.org/10.1086/191364)

Cristallo, S., Piersanti, L., & Straniero, O. 2016, in *Journal of Physics Conference Series*, Vol. 665, *Journal of Physics Conference Series* (IOP), 012019, doi: [10.1088/1742-6596/665/1/012019](https://doi.org/10.1088/1742-6596/665/1/012019)

Cristallo, S., Straniero, O., Gallino, R., et al. 2009, *ApJ*, 696, 797, doi: [10.1088/0004-637X/696/1/797](https://doi.org/10.1088/0004-637X/696/1/797)

Cristallo, S., Straniero, O., Piersanti, L., & Gobrecht, D. 2015, *ApJS*, 219, 40, doi: [10.1088/0067-0049/219/2/40](https://doi.org/10.1088/0067-0049/219/2/40)

Cseh, B., Lugaro, M., D’Orazi, V., et al. 2018, *A&A*, 620, A146, doi: [10.1051/0004-6361/201834079](https://doi.org/10.1051/0004-6361/201834079)

de Castro, D. B., Pereira, C. B., Roig, F., et al. 2016, *MNRAS*, 459, 4299, doi: [10.1093/mnras/stw815](https://doi.org/10.1093/mnras/stw815)

Delgado Mena, E., Tsantaki, M., Adibekyan, V. Z., et al. 2017, *A&A*, 606, A94, doi: [10.1051/0004-6361/201730535](https://doi.org/10.1051/0004-6361/201730535)

Doherty, C. L., Gil-Pons, P., Siess, L., & Lattanzio, J. C. 2017, *PASA*, 34, e056, doi: [10.1017/pasa.2017.52](https://doi.org/10.1017/pasa.2017.52)

El-Badry, K., Lam, C., Holl, B., et al. 2024a, *The Open Journal of Astrophysics*, 7, 100, doi: [10.33232/001c.125461](https://doi.org/10.33232/001c.125461)

El-Badry, K., Simon, J. D., Reggiani, H., et al. 2024b, *The Open Journal of Astrophysics*, 7, 27, doi: [10.33232/001c.116675](https://doi.org/10.33232/001c.116675)

El-Badry, K., Rix, H.-W., Latham, D. W., et al. 2024c, *The Open Journal of Astrophysics*, 7, 58, doi: [10.33232/001c.121261](https://doi.org/10.33232/001c.121261)

El-Badry, K., Rix, H.-W., Latham, D. W., et al. 2024d, *The Open Journal of Astrophysics*, 7, 58, doi: [10.33232/001c.121261](https://doi.org/10.33232/001c.121261)

Escorza, A., & De Rosa, R. J. 2023, *A&A*, 671, A97, doi: [10.1051/0004-6361/202244782](https://doi.org/10.1051/0004-6361/202244782)

Escorza, A., Karinkuzhi, D., Jorissen, A., et al. 2019, *A&A*, 626, A128, doi: [10.1051/0004-6361/201935390](https://doi.org/10.1051/0004-6361/201935390)

Gaia Collaboration, Vallenari, A., Brown, A. G. A., et al. 2023a, *A&A*, 674, A1, doi: [10.1051/0004-6361/202243940](https://doi.org/10.1051/0004-6361/202243940)

Gaia Collaboration, Arenou, F., Babusiaux, C., et al. 2023b, *A&A*, 674, A34, doi: [10.1051/0004-6361/202243782](https://doi.org/10.1051/0004-6361/202243782)

Ge, H., Webbink, R. F., Chen, X., & Han, Z. 2020, *ApJ*, 899, 132, doi: [10.3847/1538-4357/aba7b7](https://doi.org/10.3847/1538-4357/aba7b7)

Gonneau, A., Lançon, A., Trager, S. C., et al. 2016, *A&A*, 589, A36, doi: [10.1051/0004-6361/201526292](https://doi.org/10.1051/0004-6361/201526292)

Goswami, A., Aoki, W., Beers, T. C., et al. 2006, *MNRAS*, 372, 343, doi: [10.1111/j.1365-2966.2006.10877.x](https://doi.org/10.1111/j.1365-2966.2006.10877.x)

Gray, D. F. 2008, *The Observation and Analysis of Stellar Photospheres*

Gray, R. O., & Corbally, C. J. 1994, *AJ*, 107, 742, doi: [10.1086/116893](https://doi.org/10.1086/116893)

Gustafsson, B., Edvardsson, B., Eriksson, K., et al. 2008, *A&A*, 486, 951, doi: [10.1051/0004-6361:200809724](https://doi.org/10.1051/0004-6361:200809724)

Hallakoun, N., Shahaf, S., Mazeh, T., Toonen, S., & Ben-Ami, S. 2024, ApJL, 970, L11, doi: [10.3847/2041-8213/ad5e63](https://doi.org/10.3847/2041-8213/ad5e63)

Hansen, C. J., Nordström, B., Hansen, T. T., et al. 2016, A&A, 588, A37, doi: [10.1051/0004-6361/201526895](https://doi.org/10.1051/0004-6361/201526895)

Hansen, T. T., Andersen, J., Nordström, B., et al. 2016, A&A, 588, A3, doi: [10.1051/0004-6361/201527409](https://doi.org/10.1051/0004-6361/201527409)

Hayden, M. R., Bovy, J., Holtzman, J. A., et al. 2015, ApJ, 808, 132, doi: [10.1088/0004-637X/808/2/132](https://doi.org/10.1088/0004-637X/808/2/132)

Hegedűs, V., Mészáros, S., Jofré, P., et al. 2023, A&A, 670, A107, doi: [10.1051/0004-6361/202244813](https://doi.org/10.1051/0004-6361/202244813)

Howard, A. W., Johnson, J. A., Marcy, G. W., et al. 2010, ApJ, 721, 1467, doi: [10.1088/0004-637X/721/2/1467](https://doi.org/10.1088/0004-637X/721/2/1467)

Jermyn, A. S., Bauer, E. B., Schwab, J., et al. 2023, ApJS, 265, 15, doi: [10.3847/1538-4365/aca8d](https://doi.org/10.3847/1538-4365/aca8d)

Jofré, P., Heiter, U., Soubiran, C., et al. 2014, A&A, 564, A133, doi: [10.1051/0004-6361/201322440](https://doi.org/10.1051/0004-6361/201322440)

Jonsell, K., Barklem, P. S., Gustafsson, B., et al. 2006, A&A, 451, 651, doi: [10.1051/0004-6361:20054470](https://doi.org/10.1051/0004-6361:20054470)

Jorissen, A., Boffin, H. M. J., Karinkuzhi, D., et al. 2019, A&A, 626, A127, doi: [10.1051/0004-6361/201834630](https://doi.org/10.1051/0004-6361/201834630)

Jorissen, A., & Mayor, M. 1988, A&A, 198, 187

Kaufer, A., Stahl, O., Tubbesing, S., et al. 1999, The Messenger, 95, 8

Kelson, D. D. 2003, PASP, 115, 688, doi: [10.1086/375502](https://doi.org/10.1086/375502)

Kelson, D. D., Illingworth, G. D., van Dokkum, P. G., & Franx, M. 2000, ApJ, 531, 159, doi: [10.1086/308445](https://doi.org/10.1086/308445)

Kennedy, C. R., Sivarani, T., Beers, T. C., et al. 2011, AJ, 141, 102, doi: [10.1088/0004-6256/141/3/102](https://doi.org/10.1088/0004-6256/141/3/102)

Lambert, D. L., Gustafsson, B., Eriksson, K., & Hinkle, K. H. 1986, ApJS, 62, 373, doi: [10.1086/191145](https://doi.org/10.1086/191145)

Lau, H. H. B., Doherty, C. L., Gil-Pons, P., & Lattanzio, J. C. 2011, in Astronomical Society of the Pacific Conference Series, Vol. 445, Why Galaxies Care about AGB Stars II: Shining Examples and Common Inhabitants, ed. F. Kerschbaum, T. Lebzelter, & R. F. Wing, 45

Li, H., Aoki, W., Matsuno, T., et al. 2022, ApJ, 931, 147, doi: [10.3847/1538-4357/ac6514](https://doi.org/10.3847/1538-4357/ac6514)

Lucatello, S., Tsangarides, S., Beers, T. C., et al. 2005, ApJ, 625, 825, doi: [10.1086/428104](https://doi.org/10.1086/428104)

Lugardo, M., Herwig, F., Lattanzio, J. C., Gallino, R., & Straniero, O. 2003, ApJ, 586, 1305, doi: [10.1086/367887](https://doi.org/10.1086/367887)

Masseron, T., Johnson, J. A., Plez, B., et al. 2010, A&A, 509, A93, doi: [10.1051/0004-6361/200911744](https://doi.org/10.1051/0004-6361/200911744)

McClure, R. D. 1983, ApJ, 268, 264, doi: [10.1086/160951](https://doi.org/10.1086/160951)

McClure, R. D., Fletcher, J. M., & Nemec, J. M. 1980, ApJL, 238, L35, doi: [10.1086/183252](https://doi.org/10.1086/183252)

McKenzie, M., Yong, D., Marino, A. F., et al. 2022, MNRAS, 516, 3515, doi: [10.1093/mnras/stac2254](https://doi.org/10.1093/mnras/stac2254)

Mucciarelli, A. 2011, A&A, 528, A44, doi: [10.1051/0004-6361/201015814](https://doi.org/10.1051/0004-6361/201015814)

Nissen, P. E., & Schuster, W. J. 2011, A&A, 530, A15, doi: [10.1051/0004-6361/201116619](https://doi.org/10.1051/0004-6361/201116619)

Norris, J. E., Ryan, S. G., & Beers, T. C. 1997, ApJ, 488, 350, doi: [10.1086/304695](https://doi.org/10.1086/304695)

Norris, J. E., & Yong, D. 2019, ApJ, 879, 37, doi: [10.3847/1538-4357/ab1f84](https://doi.org/10.3847/1538-4357/ab1f84)

Parsons, S. G., Agurto-Gangas, C., Günsche, B. T., et al. 2015, MNRAS, 449, 2194, doi: [10.1093/mnras/stv382](https://doi.org/10.1093/mnras/stv382)

Pavlenko, Y. V., Jenkins, J. S., Jones, H. R. A., Ivanyuk, O., & Pinfield, D. J. 2012, MNRAS, 422, 542, doi: [10.1111/j.1365-2966.2012.20629.x](https://doi.org/10.1111/j.1365-2966.2012.20629.x)

Paxton, B., Bildsten, L., Dotter, A., et al. 2011, ApJS, 192, 3, doi: [10.1088/0067-0049/192/1/3](https://doi.org/10.1088/0067-0049/192/1/3)

Paxton, B., Cantiello, M., Arras, P., et al. 2013, ApJS, 208, 4, doi: [10.1088/0067-0049/208/1/4](https://doi.org/10.1088/0067-0049/208/1/4)

Paxton, B., Marchant, P., Schwab, J., et al. 2015, ApJS, 220, 15, doi: [10.1088/0067-0049/220/1/15](https://doi.org/10.1088/0067-0049/220/1/15)

Paxton, B., Schwab, J., Bauer, E. B., et al. 2018, ApJS, 234, 34, doi: [10.3847/1538-4365/aaa5a8](https://doi.org/10.3847/1538-4365/aaa5a8)

Paxton, B., Smolec, R., Schwab, J., et al. 2019, ApJS, 243, 10, doi: [10.3847/1538-4365/ab2241](https://doi.org/10.3847/1538-4365/ab2241)

Ramírez, I., Allende Prieto, C., & Lambert, D. L. 2013, ApJ, 764, 78, doi: [10.1088/0004-637X/764/1/78](https://doi.org/10.1088/0004-637X/764/1/78)

Ramírez, I., Meléndez, J., Bean, J., et al. 2014, A&A, 572, A48, doi: [10.1051/0004-6361/201424244](https://doi.org/10.1051/0004-6361/201424244)

Reggiani, H., Meléndez, J., Kobayashi, C., Karakas, A., & Placco, V. 2017, A&A, 608, A46, doi: [10.1051/0004-6361/201730750](https://doi.org/10.1051/0004-6361/201730750)

Rekhi, P., Ben-Ami, S., Hallakoun, N., et al. 2024, ApJL, 973, L56, doi: [10.3847/2041-8213/ad77b9](https://doi.org/10.3847/2041-8213/ad77b9)

Rekhi, P., Shahaf, S., Ben-Ami, S., et al. 2025, arXiv e-prints, arXiv:2509.13413, doi: [10.48550/arXiv.2509.13413](https://doi.org/10.48550/arXiv.2509.13413)

Rossi, S., Beers, T. C., & Sneden, C. 1999, in Astronomical Society of the Pacific Conference Series, Vol. 165, The Third Stromlo Symposium: The Galactic Halo, ed. B. K. Gibson, R. S. Axelrod, & M. E. Putman, 264

Sevilla, J., Behmard, A., & Fuller, J. 2022, MNRAS, 516, 3354, doi: [10.1093/mnras/stac2436](https://doi.org/10.1093/mnras/stac2436)

Shahaf, S., Hallakoun, N., Mazeh, T., et al. 2024, MNRAS, 529, 3729, doi: [10.1093/mnras/stae773](https://doi.org/10.1093/mnras/stae773)

Shahaf, S., Mazeh, T., Faigler, S., & Holl, B. 2019, MNRAS, 487, 5610, doi: [10.1093/mnras/stz1636](https://doi.org/10.1093/mnras/stz1636)

Siess, L. 2010, A&A, 512, A10, doi: [10.1051/0004-6361/200913556](https://doi.org/10.1051/0004-6361/200913556)

Skúladóttir, Á., Tolstoy, E., Salvadori, S., et al. 2015, A&A, 574, A129, doi: [10.1051/0004-6361/201424782](https://doi.org/10.1051/0004-6361/201424782)

Smiljanic, R., Porto de Mello, G. F., & da Silva, L. 2007, *A&A*, 468, 679, doi: [10.1051/0004-6361:20065867](https://doi.org/10.1051/0004-6361:20065867)

Sneden, C., Bean, J., Ivans, I., Lucatello, S., & Sobeck, J. 2012, MOOG: LTE line analysis and spectrum synthesis,, Astrophysics Source Code Library, record ascl:1202.009

Sneden, C. A. 1973, PhD thesis, University of Texas, Austin

Soberman, G. E., Phinney, E. S., & van den Heuvel, E. P. J. 1997, *A&A*, 327, 620, doi: [10.48550/arXiv.astro-ph/9703016](https://doi.org/10.48550/arXiv.astro-ph/9703016)

Spite, M., Caffau, E., Bonifacio, P., et al. 2013, *A&A*, 552, A107, doi: [10.1051/0004-6361/201220989](https://doi.org/10.1051/0004-6361/201220989)

Straniero, O., Gallino, R., & Cristallo, S. 2006, *NuPhA*, 777, 311, doi: [10.1016/j.nuclphysa.2005.01.011](https://doi.org/10.1016/j.nuclphysa.2005.01.011)

Temmink, K. D., Pols, O. R., Justham, S., Istrate, A. G., & Toonen, S. 2023, *A&A*, 669, A45, doi: [10.1051/0004-6361/202244137](https://doi.org/10.1051/0004-6361/202244137)

Yamaguchi, N., El-Badry, K., Rees, N. R., et al. 2024a, *PASP*, 136, 084202, doi: [10.1088/1538-3873/ad6809](https://doi.org/10.1088/1538-3873/ad6809)

Yamaguchi, N., El-Badry, K., & Shahaf, S. 2025, *PASP*, 137, 104205, doi: [10.1088/1538-3873/ae0d30](https://doi.org/10.1088/1538-3873/ae0d30)

Yamaguchi, N., El-Badry, K., & Sorabella, N. M. 2024b, *PASP*, 136, 124202, doi: [10.1088/1538-3873/ad9955](https://doi.org/10.1088/1538-3873/ad9955)

Yamaguchi, N., El-Badry, K., Fuller, J., et al. 2024c, *MNRAS*, 527, 11719, doi: [10.1093/mnras/stad4005](https://doi.org/10.1093/mnras/stad4005)

Yang, G., Zhao, J., Liang, Y., et al. 2024, *MNRAS*, 534, 3104, doi: [10.1093/mnras/stae2283](https://doi.org/10.1093/mnras/stae2283)

Zhang, L., Karlsson, T., Christlieb, N., et al. 2011, *A&A*, 528, A92, doi: [10.1051/0004-6361/201015226](https://doi.org/10.1051/0004-6361/201015226)

Zhang, X., Green, G. M., & Rix, H.-W. 2023, *MNRAS*, 524, 1855, doi: [10.1093/mnras/stad1941](https://doi.org/10.1093/mnras/stad1941)

Zorotovic, M., Schreiber, M. R., & Gänsicke, B. T. 2011, *A&A*, 536, A42, doi: [10.1051/0004-6361/201116626](https://doi.org/10.1051/0004-6361/201116626)

Zorotovic, M., Schreiber, M. R., Gänsicke, B. T., & Nebot Gómez-Morán, A. 2010, *A&A*, 520, A86, doi: [10.1051/0004-6361/200913658](https://doi.org/10.1051/0004-6361/200913658)